Remote Sensing of Environment 297 (2023) 113787

Contents lists available at ScienceDirect

Remote Sensing of Environment

journal homepage: www.elsevier.com/locate/rse

Detection of forest windthrows with bitemporal COSMO-SkyMed and Sentinel-1 SAR data

Michele Dalponte [a,*], Yady Tatiana Solano-Correa [b], Daniele Marinelli [a], Sicong Liu [c], Naoto Yokoya [d], Damiano Gianelle [a]

[a] Research and Innovation Centre, Fondazione Edmund Mach, via E. Mach 1, 38098 San Michele all'Adige, Italy
[b] Universidad Tecnológica de Bolívar, Parque Industrial y Tecnológico Carlos Vélez Pombo Km 1 Vía Turbaco, 130010 Cartagena, Colombia
[c] College of Surveying and Geoinformatics, Tongji University, 200092 Shanghai, China
[d] Department of Complexity Science and Engineering, Graduate School of Frontier Sciences, the University of Tokyo, Chiba 277–8561, Japan

ARTICLE INFO

Edited by Dr. Marie Weiss

Keywords:
SAR
Forests
Disturbances
Windthrows
Multitemporal data
Change detection

ABSTRACT

Wind represents a primary source of disturbances in forests, necessitating an assessment of the resulting damage to ensure appropriate forest management. Remote sensing, encompassing both active and passive techniques, offers a valuable and efficient approach for this purpose, enabling coverage of large areas while being cost-effective. Passive remote sensing data could be affected by the presence of clouds, unlike active systems such as Synthetic Aperture Radar (SAR) which are relatively less affected. Therefore, this study aims to explore the utilization of bitemporal SAR data for windthrow detection in mountainous regions. Specifically, we investigated how the detection outcomes vary based on three factors: i) the SAR wavelength (X-band or C-band), ii) the acquisition period of the pre- and post-event images (summer, autumn, or winter), and iii) the forest type (evergreen vs. deciduous). Our analysis considers two SAR satellite constellations: COSMO-SkyMed (band-X, with a pixel spacing of 2.5 m and 10 m) and Sentinel-1 (band-C, with a pixel spacing of 10 m). We focused on three study sites located in the Trentino-South Tyrol region of Italy, which experienced significant forest damage during the Vaia storm from 27th to 30th October 2018. To accomplish our objectives, we employed a detail-preserving, scale-driven approach for change detection in bitemporal SAR data. The results demonstrate that: i) the algorithm exhibits notably better performance when utilizing X-band data, achieving a highest kappa accuracy of 0.473 and a balanced accuracy of 76.1%; ii) the pixel spacing has an influence on the accuracy, with COSMO-SkyMed data achieving kappa values of 0.473 and 0.394 at pixel spacings of 2.5 m and 10 m, respectively; iii) the post-event image acquisition season significantly affects the algorithm's performance, with summer imagery yielding superior results compared to winter imagery; and iv) the forest type (evergreen vs. deciduous) has a noticeable impact on the results, particularly when considering autumn/winter data.

1. Introduction

Forest environments experience numerous natural disturbances that play a crucial role in their natural regeneration and adaptation. In Europe, wind stands out as the leading cause of over 50% of primary damage to forest ecosystems (Patacca et al., 2023; Sanginés de Cárcer et al., 2021). While windthrows contribute to the natural regeneration of forests, they also impose significant economic losses when viewed from an economic standpoint. Windthrows can have varying impacts, affecting both small forest patches and/or individual trees as well as the broader landscape. The extent of these impacts depends on the severity of the storm and other environmental conditions. Trees can suffer different degrees of damage, ranging from broken branches to complete uprooting. Certain studies have attempted to rank tree species based on their susceptibility to wind, although such classifications should be interpreted cautiously due to the influence of specific environmental conditions in which each species grows (Quine et al., 2021). Furthermore, the severity of damage is also influenced by various factors, including topography, soil conditions (such as soil water content, depth, and organic matter), presence of permafrost, stand conditions (such as vertical and horizontal structures, and species composition), and management activities (Albrecht et al., 2012; Jalkanen and Mattila, 2000;

* Corresponding author.
E-mail address: michele.dalponte@fmach.it (M. Dalponte).

https://doi.org/10.1016/j.rse.2023.113787
Received 20 December 2022; Received in revised form 11 August 2023; Accepted 22 August 2023
Available online 29 August 2023

Mitchell, 2013; Schelhaas, 2008; Seidl et al., 2014).

As a result of climate change, it is anticipated that windthrow events will become more frequent in the future (Seidl et al., 2014). Consequently, there is a pressing need to develop systems capable of detecting and assessing damage caused by these events. From a management standpoint, it is crucial to identify the areas affected by windthrows in order to effectively harvest the damaged trees. This is particularly important because windthrow events can trigger subsequent natural events, such as bark beetle outbreaks, that significantly exacerbate forest loss. Therefore, it is imperative to rapidly map the extent of damage in close proximity to the event, enabling forest managers to take prompt action. The accuracy of such mapping efforts is of utmost importance and strongly reliant on the availability of data to quantify the impacts of natural disasters. However, acquiring such data is typically challenging and time-consuming, often incurring substantial costs. Consequently, any alternative approach that can provide a preliminary assessment without significant time and financial burdens is advantageous.

Remote sensing emerges as a highly valuable tool for detecting forest windthrows, particularly with the advent of new satellite constellations. These satellite systems offer daily or weekly coverage, enabling swift mapping of windthrows in the aftermath of an event. Furthermore, the latest generation of sensors exhibits very high spatial resolution, facilitating precise and detailed mapping even for small-scale events. Numerous studies in the literature have leveraged various remote sensing data types and temporal approaches, such as single post-event images or multitemporal images encompassing the pre- and post-event periods (Dalponte et al., 2020; Einzmann et al., 2017; Jonikavičius and Mozgeris, 2013; Rich et al., 2010; Rüetschi et al., 2019; Schwarz et al., 2003). Among the different data sources, satellite optical images, especially multitemporal images, have been extensively employed for forest windthrow detection (Chirici et al., 2019; Dalponte et al., 2020; Einzmann et al., 2017; Jonikavičius and Mozgeris, 2013; Kislov and Korznikov, 2020; Nyström et al., 2014; Pirotti et al., 2016; Schwarz et al., 2003; Vorovencii, 2014; Wang and Xu, 2010). However, several studies have also utilized airborne data (Deigele et al., 2020; Hamdi et al., 2019; Wang and Xu, 2010) or data captured by unmanned aerial vehicles (UAVs) (Duan et al., 2017; Einzmann et al., 2017).

The use of remote sensing data, particularly optical data, can encounter limitations due to weather conditions. Cloud cover or haze can significantly impact the quality of the data, sometimes rendering it entirely unusable. Additionally, when windthrow events occur in mountainous regions during autumn or winter, low sun angles can generate extensive shadow areas in optical data, further complicating the analysis. In a recent study, (Dalponte et al., 2020), these challenges were highlighted. The researchers demonstrated that while Sentinel-2 and Planet images could deliver highly detailed windthrow detections under optimal acquisition conditions (such as using summer images before and after the event), their performance significantly declined when employing autumn or winter pre- and post-event images. This issue becomes particularly critical during emergency situations when immediate action must be taken following the occurrence of the event.

Synthetic Aperture Radar (SAR) data presents a potential solution to address the aforementioned challenges. Several studies have successfully utilized SAR data for windthrow detection (Eriksson et al., 2012; Fransson et al., 2002; Green, 1998; Lazecky et al., 2021; Rüetschi et al., 2019; Schwarz et al., 2003; Tanase et al., 2018; Thiele et al., 2012; Ulander et al., 2005; Vaglio Laurin et al., 2021). Green (1998) conducted an analysis using different SAR images acquired from airborne platforms in L-band and C-band, considering four polarizations (HH, HV, VH, and VV). The study revealed that co-polarized backscatter (HH, VV) exhibited greater sensitivity to canopy gaps compared to cross-polarized (HV, VH), with C-band demonstrating potential as the most useful wavelength due to its larger dynamic range in backscatter compared to L-band. Additionally, the study identified significant relationships between the shape of canopy gaps (measured by area, perimeter, and perimeter/area ratio) and resulting backscatter. Rüetschi et al. (2019) employed Sentinel-1C-band VV and VH polarimetric data to detect forest windthrows in Switzerland and Germany. They achieved high detection accuracy, with user's and producer's accuracy reaching approximately 85% for locating windthrow areas. However, the results were less accurate when detecting individual windthrown trees. Tanase et al. (2018) utilized ALOS L-band data for forest windthrow detection and achieved high levels of accuracy (up to 90%) using image thresholding as the detection approach. SAR data have also been widely employed for change detection purposes, including the detection of forest fires (Abdikan et al., 2022; Ban et al., 2020; Belenguer-Plomer et al., 2021; Bovolo and Bruzzone, 2005; Hosseini and Lim, 2023). Various SAR satellites are currently operational, such as Sentinel-1, ALOS-2, SAOCOM, ICEYE, Capella, TerraSAR-X and Tandem-X, RADARSAT, and COSMO-SkyMed. Some of these satellites or constellations provide high spatial resolution data, which can be advantageous for detailed windthrow patch detection. Additionally, the COSMO-SkyMed constellation offers the potential for acquiring two images per day, one in the ascending and one in the descending direction, thereby increasing the probability of conducting a comprehensive analysis of affected areas.

The use of SAR data in mountainous areas encounters significant limitations, including foreshortening, layover, and shadows, as outlined in previous studies (Chen et al., 2018; Cigna et al., 2014; Wu et al., 2021). Foreshortening occurs when the radar beam reaches the base of an inclined tall feature, such as a mountain slope, before reaching its top, resulting in an inaccurate representation of the slope length. Layover, on the other hand, arises when the radar beam reaches the top of a tall feature before reaching its base. Shadows in SAR images occur when higher objects obstruct the radar beam, preventing it from illuminating certain areas. As a result, shadowed regions appear dark in the image due to the absence of backscattered energy. The extent of shadow effects increases as the radar beam's incidence angle becomes more oblique with respect to the surface. Given that forested areas often cover mountainous regions, the use of SAR data in such areas can pose challenges. One approach to partially overcome this issue is to combine multiple SAR images acquired from different viewing directions (Bernardi et al., 2021; Horch et al., 2019; Wu et al., 2021). By leveraging acquisitions with varying viewing directions, different shadowed areas can be captured. For instance, in a mountainous area, a different acquisition direction may shift the shadowed area from one side of a valley to the other. By integrating multiple acquisitions, it becomes possible to achieve broader coverage of the area of interest with useful data. Many SAR satellite constellations offer the opportunity to combine ascending and descending data, enabling this approach.

Despite the existing literature on windthrow detection using remote sensing data, certain aspects, particularly regarding the use of SAR data in mountainous areas, have remained unexplored. The primary objective of this study is to investigate the effectiveness of multitemporal SAR data, acquired in both X and C bands (specifically COSMO-SkyMed and Sentinel-1 data), for detecting windthrows in mountainous regions. In particular, this study aims to examine the influence of the following factors on the detection results: i) SAR wavelength (C-band and X-band), ii) pixel spacing, iii) acquisition period, and iv) forest types (evergreen vs all). The impact of forest types is of particular importance, especially in cases where windthrows predominantly affect evergreen trees and occur during autumn in areas characterized by the presence of broadleaved species (Udali et al., 2021). Under such circumstances, the leaf-off conditions of trees in the post-event image may introduce an additional change that could potentially be mistaken for windthrow damage (Rüetschi et al., 2019).

2. Data set description

2.1. Study area

The study area encompasses the administrative districts of the

Fiemme and Fassa valleys, located in the North-East part of the Autonomous Province of Trento (PAT) in Italy (Fig. 1). It spans a total area of 732 km^2, with approximately 454 km^2 covered by forests. The topography of the region is predominantly mountainous, and the most prevalent tree species include Norway spruce (*Picea abies* (L.) H. Karst), silver fir (*Abies alba* Mill.) and European beech (*Fagus sylvatica* L.). In late October 2018, the area, along with the entire Northeast of Italy, experienced the devastating Vaia storm, which stands out as one of the most severe storm events to occur in Italy in recent decades (Giovannini et al., 2021). The storm brought heavy precipitation and snowfall at higher altitudes, accompanied by strong winds reaching speeds of up to 200 km/h. The consequences for the forests in the study area were significant. Within our defined study area, a total of 46 km^2 of forested land suffered damage out of the 454 km^2 that were initially forested (Servizio Foreste e Fauna - Provincia Autonoma di Trento, 2018). Approximately 65% of the damaged areas were dominated by Norway spruce, 17% by silver fir, 6% by pines, 5% by European beech, 4% by larch, and 3% by other species (Servizio Foreste e Fauna - Provincia Autonoma di Trento, 2018).

2.2. Reference data

The reference data used for windthrows detection were obtained from three specific areas. The delineation of windthrows was carried out through manual photointerpretation using high-resolution imagery. Two SPOT-7 images with a spatial resolution of 1.5 m, captured on 17 and 28 November 2018, were utilized for the initial mapping. Additionally, four Dove images with a spatial resolution of 3 m, acquired before (two images: 23 June 2018 and 22 October 2018) and after (14 November 2018 and 26 June 2019) the windthrows event, were used to refine the mapping in the areas shadowed or covered by snow in the SPOT-7 images. The minimum mapping unit was driven by the pixel size of the images used in the photointerpretation: the smallest area mapped was 9 m^2, the largest 1,746,189 m^2, the mean value was 6433 m^2, and the median 396 m^2. Fig. 1 displays the three designated areas where windthrows were delineated, and their specific characteristics are presented in Table 1. The main distinguishing factors among the three areas are the variation in the percentage of deciduous forest types and the variation in median aspect of the covered terrain.

2.3. COSMO-SkyMed data

COSMO-SkyMed (COnstellation of small Satellites for the Mediterranean basin Observation) is a space-based satellite SAR constellation managed by the Italian Space Agency (ASI).[1] This constellation consists of four medium-sized satellites (approximately 1700 kg) that provide global coverage. The satellites can collect observations on-demand and can revisit an area of interest twice a day, regardless of weather conditions. The SAR data acquired by COSMO-SkyMed can be obtained in both single- and dual-polarization, specifically in the X-band. The spatial resolution varies depending on the acquisition modes. In this study, archived data were utilized, with different images selected for each study site (refer to Table 2). Whenever possible, images were chosen from periods without heavy precipitations events, as illustrated in Fig. 2. All the images were acquired in the Stripmap HIMAGE mode in the HH polarization. The images were provided by ASI through the COSMO-SkyMed Open Call for Science in the processing level 1B - Detected Ground Multi-look (DGM). The level 1B (DGM) products are obtained starting from the L1A data and they contain: focused data, detected, radiometrically equalized and in ground range/azimuth projection. The main processing steps, performed on L1A input data, are: multi-looking for speckle reduction, image detection (amplitude), and ellipsoid ground projection. The images have a range and azimuth resolution of 5 m, a pixel spacing of 2.5 m, and a swath width and scene length of 40 km (Italian Space Agency, 2019). The equivalent number of looks is slightly larger than 3 for all the images used.

2.4. Sentinel-1 data

Sentinel-1 is a satellite SAR constellation managed by the European Space Agency (ESA) inside the Copernicus programme. The constellation includes two polar-orbiting satellites with global coverage of the planet. The constellation operates in the C-band. In this study we considered data acquired in Interferometric Wide (IW) swath mode that is the predefined mode used over land areas. The polarizations used were VV and VH which are the standard polarization used outside the polar and sea-ice regions. As for the COSMO-SkyMed data, we used the Level-1 Ground Range Detected (GRD) products that consist of focused SAR data that has been detected, multi-looked and projected to ground range using the Earth ellipsoid model WGS84. Inside the Level-1 GRD products we chose the high-resolution ones (GRDH), having a swath width of 250 km, azimuth resolution of 22.5 m, a range resolution of 20.4 m, and a pixel spacing of 10 m. The equivalent number of looks is 4.4[2]. The images used in this study are summarized in Table 2 and Fig. 2.

3. Methods

3.1. Data pre-processing

Each input image (X_{PRE} and X_{POST}) was processed using the software SNAP (*SNAP - ESA Sentinel Application Platform v8.0, http://step.esa.int*). To each image, the calibration module and the range-doppler terrain correction module were applied (Fig. 3). The objective of SAR calibration is to provide imagery in which the pixel values can be directly related to the radar backscatter of the scene. Due to topographical variations of a scene and the tilt of the satellite sensor, distances can be distorted in the SAR images. Terrain corrections are intended to compensate for these distortions so that the geometric representation of the image will be as close as possible to the real world. The range-doppler terrain correction module applies both an orthorectification and a radiometric normalization. The orthorectification is done applying the method proposed by (Small and Schuber, 2008), while the radiometric normalization is based on the approach proposed by (Kellndorfer et al., 1998). The range-doppler terrain correction was done using a digital terrain model (DTM) at 2 m ground sampling distance provided by the local administration and extracted from a LiDAR survey carried out in 2015. Regarding the COSMO-SkyMed constellation we produced the images of the calibrated backscatter (sigma0 band) for the HH polarization at a pixel spacing of 2.5 m (afterward referred to as $CSK_{2.5}$) and at 10 m (afterwards referred to as CSK_{10}), while for the Sentinel-1 we produced the sigma0 bands of the VH and VV polarizations at 10 m pixel spacing (afterward referred to as $S1_{VH}$ and $S1_{VV}$). It is important to keep in mind that CSK_{10} is only an approximation of data at 10 m, since it has been generated starting from the $CSK_{2.5}$, and not originally acquired at this resolution.

Shadow and layover masks (M_{LS}) were also extracted for each input image by means of SNAP using the SAR simulation module having the same DTM, used for the terrain correction, as input. The spatial resolution of these masks was the same as the corresponding sigma0 bands. Each sigma0 band was then masked using the corresponding M_{LS}. All images were also masked using the forest/non-forest layer provided by the Forest Service of the Autonomous Province of Trento: only areas considered as forest were retained for the windthrows detection. These final images (X^P_{PRE} and X^P_{POST}) were the ones used as input to the windthrows detection algorithm.

[1] https://www.asi.it/en/earth-science/cosmo-skymed/

[2] https://sentinels.copernicus.eu/web/sentinel/technical-guides/sentinel-1-sar/products-algorithms/level-1-algorithms/ground-range-detected/iw

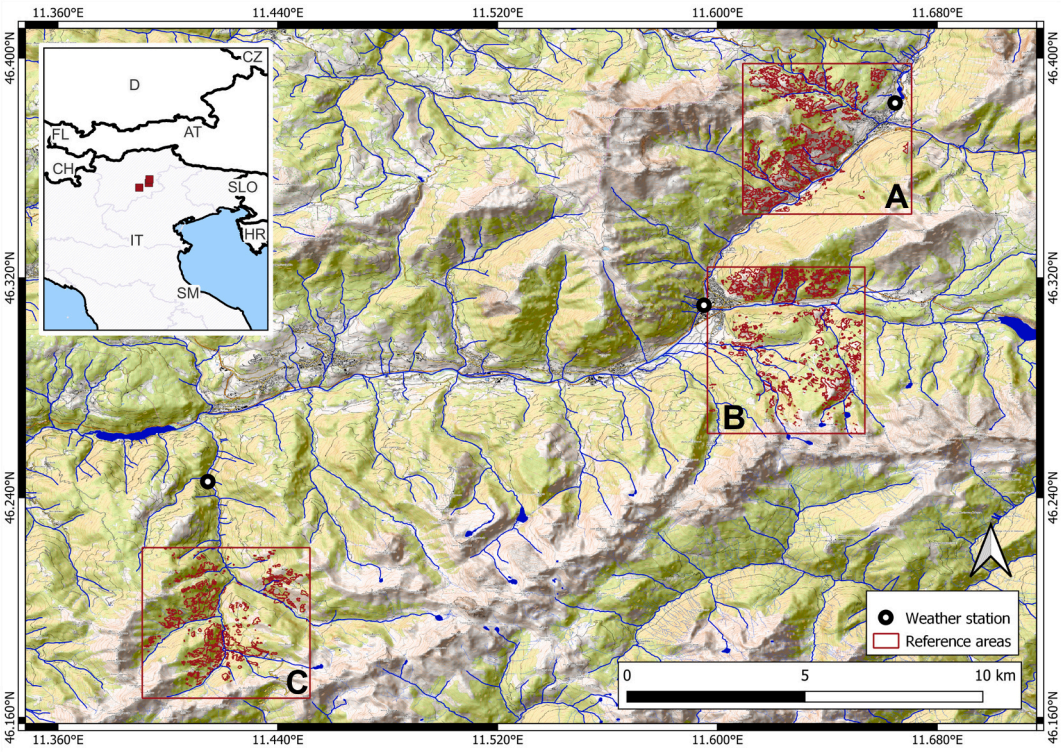

Fig. 1. Location of the three study areas. In dark-red the windthrow areas delineated by photointerpretation. In the inset the location of the study areas in Italy. (For interpretation of the references to colour in this figure legend, the reader is referred to the web version of this article.)

Table 1
Characteristics of the three study areas.

		A	B	C
Area (km^2)	Non-forest	6.1	3.9	3.9
	Intact forest	16.3	20.9	20.7
	Windthrows	5.0	3.1	2.8
	Total	27.4	27.9	27.4
Windthrows patches	Number	456	774	426
	Area range (m^2)	36–1,746,189	9–389,781	9–737,316
	Median area (m^2)	472.5	288	567
Altitude a.s.l. (m)	Range	1095–2318	989–2291	1142–2487
	Median	1513	1511	1808
Slope (°)	Range	0.003–77.7	0.009–79.2	0.255–77.8
	Median	29.7	24.9	31.0
Aspect (°)	Range	0–360	0–360	0–360
	Median	154.8	233.8	193.4
Forest types (%)	Deciduous	12.2	5.4	24.2
	Evergreen	87.8	94.6	75.8

3.2. Windthrows detection

The proposed windthrows detection methodology was developed based on the change detection method proposed by Bovolo and Bruzzone (2005) to detect forest fires using ERS-1 SAR data. The proposed windthrows detection is organised into four steps: i) creation of the log-ratio image; ii) multiscale decomposition/reconstruction; iii) Otsu thresholding of each multiscale component; and iv) final decision using a majority rule for each pixel.

3.2.1. Creation of the log-ratio image

In contrast to what happens in optical data when performing multitemporal analysis, SAR data cannot be directly compared by a univariate image difference because of the speckle noise present in these images that changes the statistical distribution of the data. The comparison is then made by a ratio operation, instead of a subtraction one. This operation not only helps to reduce the speckle effects, but also to have independent absolute intensity with respect to the measured signal (Bovolo and Bruzzone, 2005). Since low-intensity values can be present in the images, it is common to express the ratio image in a logarithmic scale. Thus, the resulting log-ratio image X_{LR} can be defined as the logarithm of the ratio between the pre-processed post- (X^P_{POST}) and pre-event (X^P_{PRE}) images:

$$X_{LR} = log\left(\frac{X^P_{POST}}{X^P_{PRE}}\right) \quad (1)$$

In X_{LR} unchanged pixels assume values close to zero, whereas increase and decrease of backscattering assume positive and negative values far from zero, respectively.

3.2.2. Multiscale decomposition/reconstruction

Given the inherent noise present in SAR data, it is often necessary to apply spatial filtering techniques to enhance the Signal-to-Noise Ratio (SNR) of the images. However, such filtering operations typically lead to a trade-off between noise reduction in homogeneous areas and loss of spatial details. To address this challenge and preserve spatial details while reducing noise in homogeneous regions, a viable solution is to analyse the data at multiple spatial scales. This approach allows for noise reduction while retaining sensitivity to geometric details (Marin et al., 2015). The multiscale analysis involves examining the image at various levels of spatial resolution. High-resolution levels are utilized for analysing geometric details, while low-resolution levels provide insights into homogeneous areas. Specifically, low-resolution levels furnish information about the windthrow's location and approximate extent, while high-resolution levels supply the necessary geometric details to delineate area boundaries and detect subtle changes. Various methods can be employed to achieve multiscale decomposition, such as Laplacian/Gaussian pyramid decomposition, wavelet transform, recursively up-sampled bicubic filter, among others. In this study, we adopted a

Table 2
COSMO-SkyMed and Sentinel-1 images used in this study for each study area. ASC = Ascending; DSC = Descending; Pre = pre-event; Post = post-event. The incidence angle values are the maximum and minimum inside the area.

Area	Direction	Time	Season	COSMO-SkyMed			Sentinel-1		
				Date	Incidence angle	Layover/ Shadow area (%)	Date	Incidence angle	Layover/ Shadow area (%)
A	ASC	Pre	Summer	2018-08-16	26.5° - 27.1°	40.5	2018-08-17	40.1° - 40.4°	16.3
			Autumn	2018-10-19	26.6° - 27.2°	40.1	2018-10-16	40.1° - 40.4°	16.4
		Post	Winter	2018-12-06	26.6° - 27.2°	40.4	2018-11-21	40.1° - 40.4°	16.4
			Summer	2019-08-03	26.5° - 27.1°	40.5	2019-08-12	40.1° - 40.4°	16.4
	DSC	Pre	Summer	2018-08-09	31.4° - 31.9°	38.9	2018-08-16	42.9° - 43.2°	15.3
			Autumn	–	–	–	2018-10-15	42.8° - 43.2°	15.1
		Post	Winter	2018-11-29	31.4° - 31.9°	39.1	2018-11-20	42.9° - 43.2°	15.2
			Summer	2019-08-23	31.4° - 31.9°	38.6	2019-08-11	42.9° - 43.2°	15.2
B	ASC	Pre	Summer	2018-08-16	26.3° - 26.9°	48.8	2018-08-17	39.9° - 40.2°	21.1
			Autumn	2018-10-19	26.4° - 26.9°	48.7	2018-10-16	39.9° - 40.2°	20.9
		Post	Winter	2018-12-06	26.4° - 26.9°	48.7	2018-11-21	39.9° - 40.2°	21
			Summer	2019-08-03	26.3° - 26.8°	48.9	2019-08-12	39.9° - 40.2°	20.9
	DSC	Pre	Summer	2018-08-09	31.3° - 31.9°	24	2018-08-16	42.8° - 43.2°	13.7
			Autumn	–	–	–	2018-10-15	42.8° - 43.2°	13.7
		Post	Winter	2018-11-29	31.3° - 31.9°	23.9	2018-11-20	42.8° - 43.2°	13.7
			Summer	2019-08-23	31.4° - 31.9°	23.9	2019-08-11	42.8° - 43.2°	13.7
C	ASC	Pre	Summer	2018-08-15	34.0° - 34.5°	35.7	2018-08-17	38.8° - 39.2°	17.8
			Autumn	2018-10-18	34.0° - 34.5°	35.7	2018-10-16	38.8° - 39.2°	17.9
		Post	Winter	2018-11-19	34.0° - 34.5°	35.8	2018-11-21	38.8° - 39.2°	17.9
			Summer	2019-08-13	33.9° - 34.4°	35.8	2019-08-12	38.8° - 39.2°	17.9
	DSC	Pre	Summer	2018-08-09	32.4° - 32.9°	38.4	2018-08-16	43.6° - 43.9°	13.3
			Autumn	2018-10-15	32.4° - 32.8°	34.9	2018-10-15	43.6° - 43.9°	13.4
		Post	Winter	2018-11-29	32.4° - 32.8°	38.5	2018-11-20	43.6° - 43.9°	13.3
			Summer	2019-08-23	32.4° - 32.9°	38.4	2019-08-11	43.6° - 43.9°	13.4

two-dimensional discrete Stationary Wavelet Transform (2D-SWT), following the approach proposed by Bovolo and Bruzzone (2005).

In greater detail, from X_{LR} a set of multilevel (ML) images $X_{ML} = \{x_{LR}^1, \ldots, x_{LR}^N\}$ is computed, where the superscript (i.e., *1, …,N*) indicates the resolution level. This is done in two steps: a decomposition phase in which X_{LR} is filtered through a cascade of n filters, and a reconstruction phase, in which only the information of interest is used to reconstruct the original image at the n^{th} resolution level. The decomposition is based on 2D-SWT using a Daubechies wavelet family with a filter length equal to 8. For each approximation sub-band, the inverse stationary wavelet transform (2D-ISWT) is applied $n + 1$ times to reconstruct in the image space set $X_{ML} = \{x_{LR}^1, \ldots, x_{LR}^N\}$. It is worth noting that, after the reconstruction, all levels have the same pixel spacing as the pixel spacing of the input image (X_{LR}). Fig. 4 shows an example of the multiscale decomposition with 7 levels on part of the reference area A for the $CSK_{2.5}$ data. The figure clearly shows that the first high-resolution levels (i.e., $N = 1,2$) preserve all the geometrical details while remaining noisy. Therefore, the analysis of such levels results in detection maps with a high level of spatial detail at the cost of many false alarms. In contrast, low-resolution levels (i.e., N = 5, 6, 7) lose most of the high spatial frequency information but are almost noise free. Their analysis can provide detection maps, with good performance (i.e., few false alarms) in homogenous areas, that identify the locations of the windthrows, but provide little information regarding their boundaries. This highlights how all levels must be analysed in a synergistic way to fuse and exploit their different information content. Fig. 5 shows the distribution of the pixel values in the two classes in each of the 7 levels of the example in Fig. 4. The variability is much higher in the first levels, with less separability among the classes. Variability decreases while increasing the level of analysis, but separability improves at the same time.

Preliminary analyses were carried out to fix the value of the number N of levels in the Wavelet transform. The value of N was fixed at 7 for the $CSK_{2.5}$ data, while for the other experiments (CSK_{10}, $S1_{VH}$, and $S1_{VV}$) it was fixed at 5. These values were defined both according to some initial pre-analyses and according to the fact that it is expected that more levels are needed for images at higher resolution.

3.2.3. *Image thresholding and decision*

To fuse the information of the different resolution levels of X_{ML}, the images were analysed separately according to a thresholding approach followed by a fusion of the resulting binary images. The thresholding operation separated changed and unchanged pixels in each level of X_{ML} and was defined using the Otsu thresholding method (Otsu, 1979). The Otsu method automatically detects the threshold, by minimizing intra-class intensity variance, or, equivalently, by maximising inter-class variance (Otsu, 1979). Depending on the SAR band, windthrows areas were identified as above or below the threshold: for the COSMO-SkyMed images (X-band) we considered as windthrows pixels with values above the Otsu threshold, while for the Sentinel-1 images (C-band) pixels with value below the threshold were considered as windthrows. More details about this choice are presented in the discussions section.

The set of maps $X_{TH} = \{x_{TH}^1, \ldots, x_{TH}^N\}$ was then fused in a single detection map using a majority rule: the pixels for which most of the

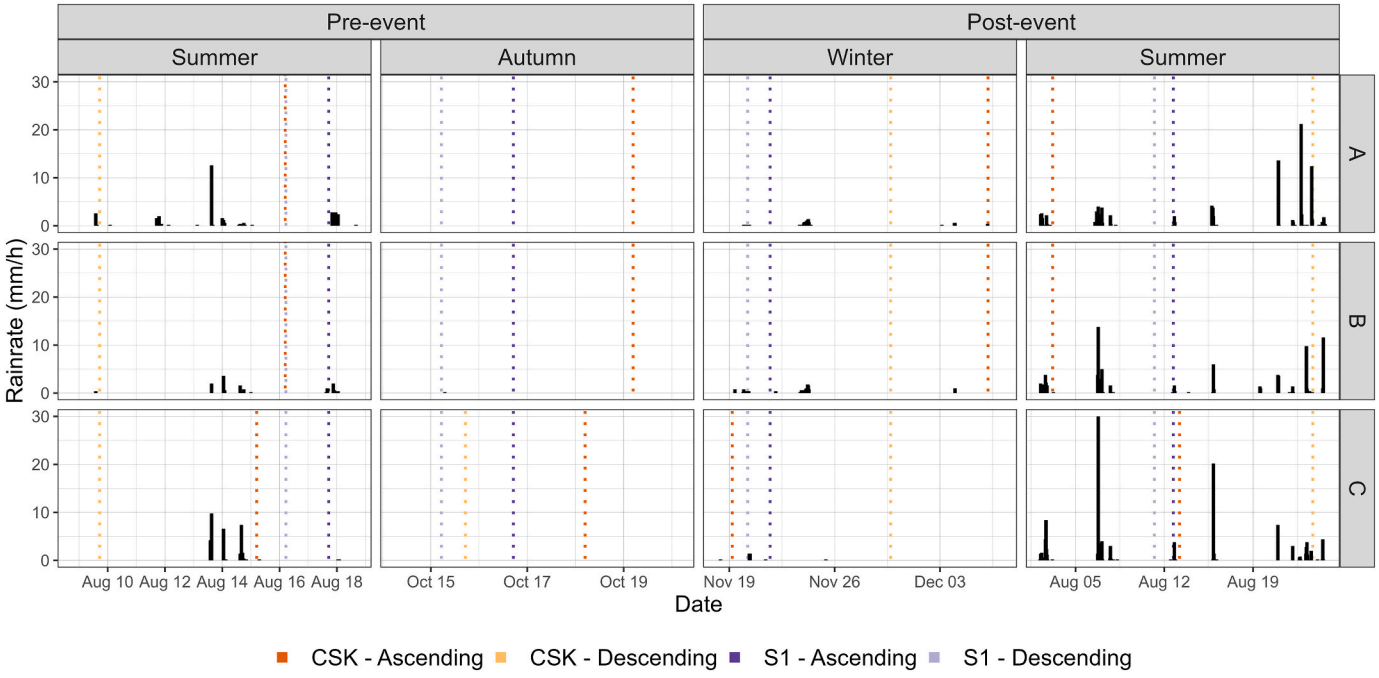

Fig. 2. Precipitations around the acquisition dates of the images for the three study areas. The precipitations values were extracted from the data measured by three weather stations located inside the three areas.
https://www.meteotrentino.it/index.html#!/content?menuItemDesktop=111

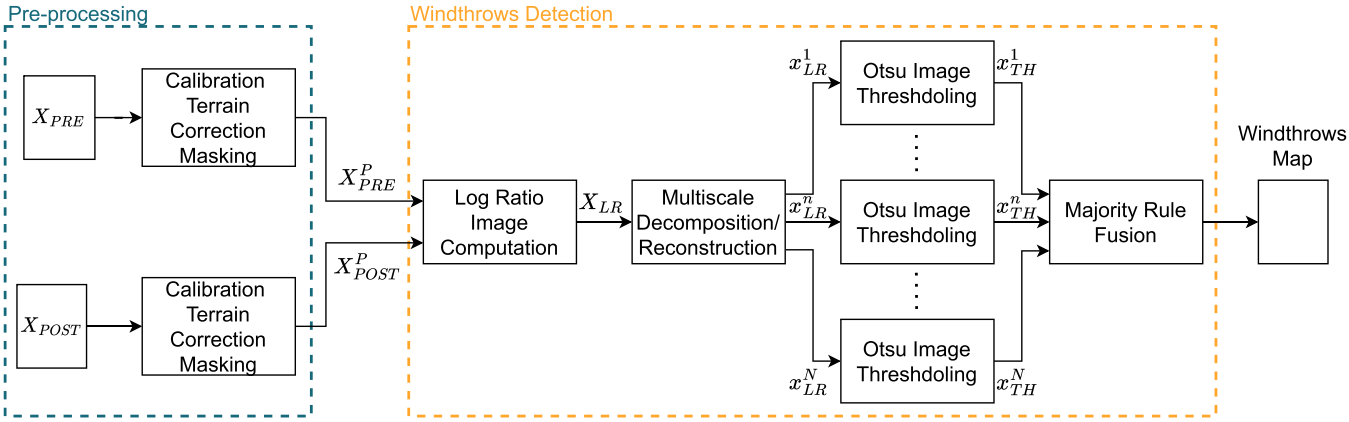

Fig. 3. Architecture of the methods adopted in this study.

maps assigned a change were considered windthrows, while the others were considered as non windthrows. In such a way, the information content of the different levels is fused preserving the geometrical details of the first levels while reducing the number of false alarms due to the better representation of homogenous areas in the lower levels. Fig. 4 bottom panel shows an example of how the binary images are fused according to a majority rule. In particular, the image clearly shows how almost all false detections caused by noise in the high levels are associated with a low number of votes. In contrast, areas with windthrows show a high number of votes in homogenous areas and a slightly smaller number of votes on the border of such areas (i.e., the areas with geometric details).

To ensure a wall-to-wall coverage of the analysed area in an operational scenario, it is necessary to generate maps using both ascending and descending data, as images acquired in these modes have different masking characteristics for layover and shadows. The merging of these maps can be performed in two ways: i) before the analysis: the original data from ascending and descending acquisitions are merged prior to the windthrow detection process; ii) after the mapping: the detection maps generated separately from ascending and descending data are merged. In this study the merging was done after the mapping.

3.3. Design of experiments

In this study, we considered four scenarios for windthrow detection based on the spatial resolution of the data and the available polarizations: i) COSMO-SkyMed images at the original pixel spacing of 2.5 m ($CSK_{2.5}$); ii) COSMO-SkyMed images resampled to the same pixel spacing as Sentinel-1 images (10 m; CSK_{10}); iii) Sentinel-1 images in VV polarization at 10 m pixel spacing ($S1_{VV}$); and iv) Sentinel-1 images in VH polarization at 10 m pixel spacing ($S1_{VH}$). For each sensor and resolution, we evaluated four combinations of pre- and post-event images based on different seasons: i) summer-winter (SW): images acquired in summer before the windthrow event and in winter after the event; ii) summer-summer (SS): images acquired in summer before and after the event; iii) autumn-winter (AW): images acquired in autumn before the

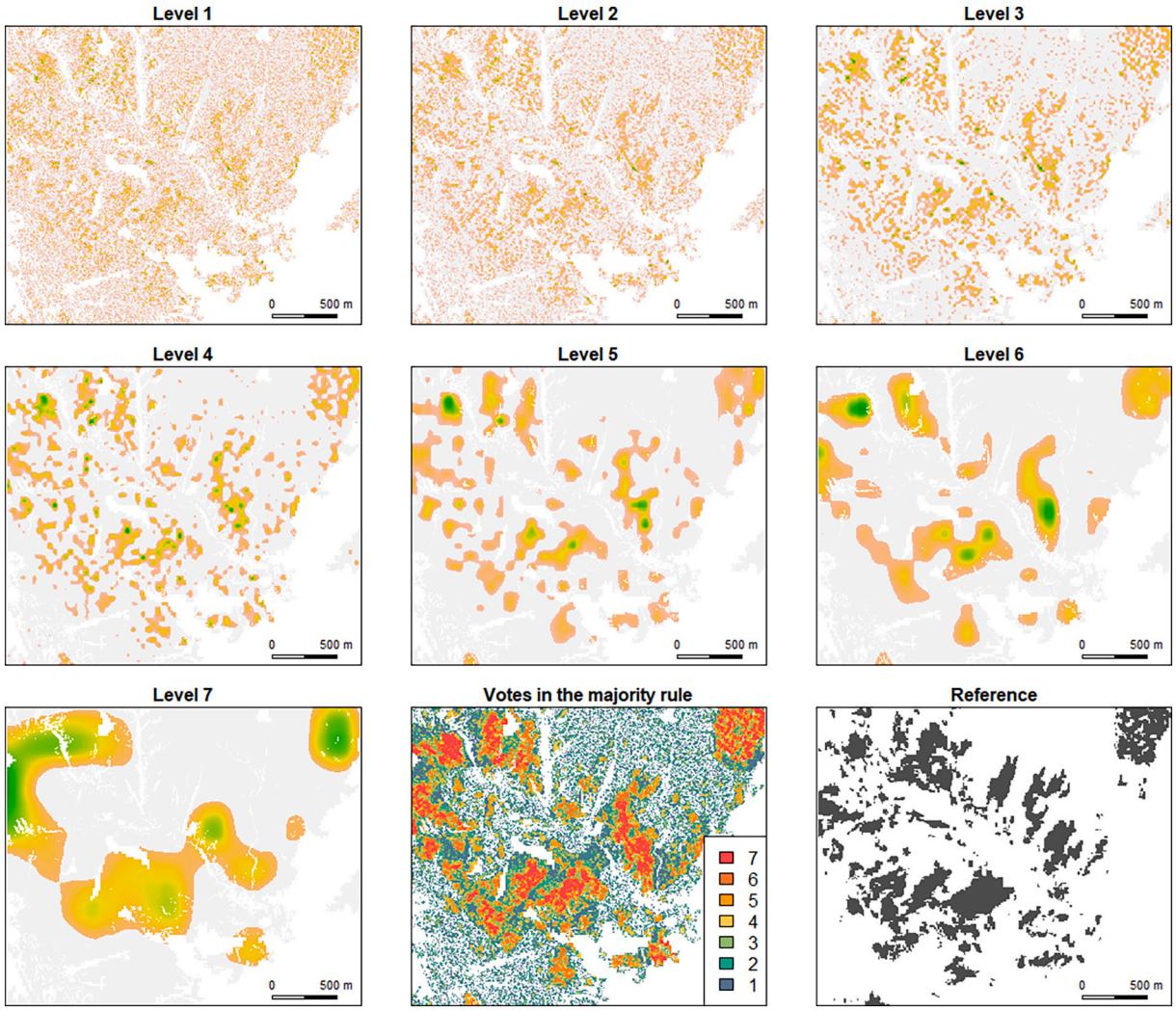

Fig. 4. Multiscale image sequence obtained by applying the decomposition/reconstruction with 7 layers over part of the reference area A on the $CSK_{2.5}$ data. The input image is the combination of ascending and descending images acquired in summer 2018 and 2019. The areas in gray are areas below the threshold and thus classified as non-windthrows.

event and in winter after the event; iv) autumn-summer (AS): images acquired in autumn before the event and in summer after the event. The rationale behind using different combinations of seasons is to address the need for timely windthrow mapping while considering potential limitations of images acquired very close to the event due to concurrent changes. Thus, we explored four combinations: one involving images closest to the event (AW); one minimizing the effects of phenology and snow cover (SS); and two intermediate combinations (SW and AS). Additionally, we considered two forest type scenarios: all forest types and only evergreen forest areas. This distinction is particularly important when windthrows predominantly affect evergreen trees and occur in autumn in areas with broadleaved species. For each combination, we produced maps separately using both ascending and descending data from the respective sensors. We then merged the two maps to create a wall-to-wall map, considering a pixel as a windthrow if it was detected as such in either the ascending or descending image. This approach allowed us to take advantage of both ascending and descending acquisitions, increasing the coverage of the windthrow detection maps.

The validation of the maps was done both at pixel and patch level using the metrics of Table 3: *RP* is defined as a windthrow patch delineated in the reference map, and *MP* as a windthrow patch mapped by the windthrows detection algorithm. The metrics used for the pixel level accuracy are the standard metrics used in change detection and automatic classification studies (Table 3). Regarding the patch level non-standard metrics have been used (Table 3). We opted to use the term "patch" instead of "polygon" as it better represents the highly fragmented windthrows areas. The application of different masks (e.g., layover/shadow and forest/non-forest masks) resulted in windthrow objects exhibiting highly irregular shapes, including potential holes. Moreover, these windthrow areas varied significantly in size, ranging from extensive regions to small fragments. To analyse the detection accuracy for small and large patches some metrics were analysed considering only patches of size lower or equal than 500 m^2, and >500 m^2 (superscripts "≤500" and ">500", respectively). $\#MP$ and MP_{AREA} are intended to indicate the amount and size of windthrows patches found by the algorithm particularly in relation to the different pixel spacings analysed. $RP_{DET}^{\leq 500}$ and $RP_{DET}^{>500}$ are used to indicate the percentage of the windthrows patches present in the reference map that had an overlap with the windthrows patches delineated by the algorithm. For both indexes, to classify a patch as detected, it is sufficient that at least one pixel of the windthrow map overlaps with a reference patch. The metrics $MP \Rightarrow RP^{\leq 500}$, $MP \Rightarrow RP^{>500}$, $RP^{\leq 500} \Rightarrow MP$ and $RP^{>500} \Rightarrow MP$ quantify: i) the degree of sub-patch splitting performed by the algorithm ($MP \Rightarrow RP^{\leq 500}$ and $MP \Rightarrow RP^{>500}$) and ii) the extent of over-detection leading to large patches encompassing multiple reference areas ($RP^{\leq 500} \Rightarrow MP$ and $RP^{>500} \Rightarrow MP$). Ideally, perfect windthrow detection

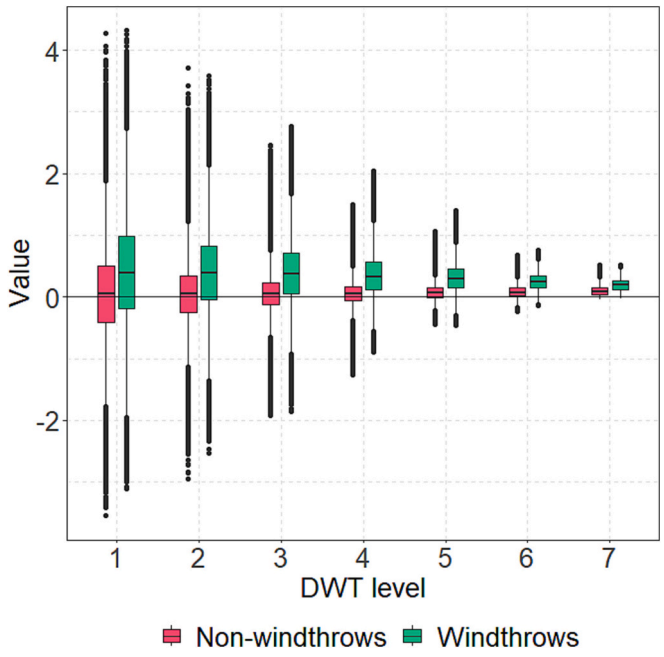

Fig. 5. Boxplots of the values of the 7 levels images of Fig. 4 separated into the two classes.

Table 3
Accuracy metrics used in this study.

Level	Acronym	Description
Pixel	K	Kappa accuracy
	BA	Balanced accuracy in %: mean value of the PAs
	PA_W	Producer's accuracy in % of the windthrows class
	PA_{NW}	Producer's accuracy in % of the non-windthrows class
	UA_W	User's accuracy in % of the windthrows class
	UA_{NW}	User's accuracy in % of the non-windthrows class
Patch	$\#MP$	The total number of windthrows mapped patches MP
	MP_{AREA}	Mean area in m^2 of the mapped patches
	$RP_{DET}^{\leq 500}$	% of the detected reference patches RP with area below or equal to 500 m^2
	$RP_{DET}^{>500}$	% of the detected reference patches RP with area above 500 m^2
	$MP \rightrightarrows RP^{\leq 500}$	Mean number of MP overlapping each RP with area below or equal to 500 m^2
	$MP \rightrightarrows RP^{>500}$	Mean number of MP overlapping each RP with area above 500 m^2
	$RP^{\leq 500} \rightrightarrows MP$	Mean number of RP with area below or equal to 500 m^2 overlapping each MP
	$RP^{>500} \rightrightarrows MP$	Mean number of RP with area above 500 m^2 overlapping each MP

would result in all four metrics equalling 1. For instance, a value of 2 for $MP \rightrightarrows RP^{>500}$ indicates that, on average, there are two mapped patches (MP) for each reference area ($RP^{>500}$).

In the computation of the accuracy metrics discussed earlier, we decided to use only the part of the maps that were not masked in any combination. Specifically, for both satellite constellations, we used ascending mode images for areas A and B, and both ascending and descending images for area C. By considering only the pixels available in all data sources, we ensured that the final maps were masked and restricted to a consistent set of data. Although this approach reduced the overall surface area analysed, it enabled us to obtain comparable results across the four data combination experiments and the two sensors. It is important to note that this masking process was exclusively applied to ensure a rigorous computation of the accuracy metrics and was not used in the generation of the maps themselves. The results presented in the paper treated the three areas as a unified area, but in the supplementary materials, we also provided separate results for each individual area.

In the experiments that incorporated forest type analysis, the study areas underwent masking based on two criteria: (1) considering all forest areas, and (2) considering forest areas predominantly composed of evergreen species. To accomplish this, we used a shapefile containing information on forest type, which was generated during the forest inventories conducted in the respective areas.

4. Results

Fig. 6 illustrates the results of windthrow detection when considering all four data sets and combinations of the four seasons. Among the various data sources, the use of summer images before and after the event yielded the highest accuracies in windthrow detection. Specifically, $CSK_{2.5}$ data demonstrated the highest accuracies, followed by CSK_{10} data (Fig. 6). The accuracies obtained from Sentinel-1 data were relatively lower, with variations observed between the VH and VV polarizations. VH polarization generally exhibited better performance compared to VV polarization. Upon closer examination of the producer's and user's accuracies, some notable trends emerged. PA_W remained relatively stable across seasons, pixel spacings, and data sources, consistently surpassing 60%. UA_{NW} consistently exceeded 75% and showed stability regardless of the seasons' combinations and data sources. However, PA_{NW} and UA_W exhibited significant variations depending on the seasons' combinations and data sources. Sentinel-1 data consistently yielded low values for PA_{NW} and UA_W, with PA_{NW} below 50% (except for the summer-summer combination with Sentinel-1 VH data) and UA_W below 30%. The only combinations that achieved PA_{NW} and UA_W values above 50% were the summer-summer combinations with COSMO-SkyMed data.

The patch-level results are presented in Fig. 7. When using $CSK_{2.5}$ and CSK_{10} data, the number of mapped patches ($\#MP$) varies depending on the post-event season, with higher values when a winter image is considered as the post-event image. The value of $\#MP$ remains relatively stable for both Sentinel-1 datasets. Conversely, MP_{AREA} is much smaller when using $CSK_{2.5}$ data (796–1016 m^2) compared to the other datasets (CSK_{10}, $S1_{VV}$ and $S1_{VH}$) (3481–7976 m^2). Similar to the previous metric, the results from the two Sentinel-1 data sources exhibited less variability (5412–7976 m^2), while it varies depending on the post-event season image for CSK_{10} data (3481 m^2 vs. 6170 m^2). $RP_{DET}^{\leq 500}$ and $RP_{DET}^{>500}$ show distinct behaviors. $RP_{DET}^{\leq 500}$ remains relatively stable for Sentinel-1 datasets, while for COSMO-SkyMed datasets, the values are significantly lower for SS and AS combinations. Similar trends were observed for $RP_{DET}^{>500}$, although the differences between SS/AS and SW/AW combinations are limited. For COSMO-SkyMed datasets, the best results for $RP_{DET}^{\leq 500}$ were obtained when a winter image was used as the post-event image (76.1% for $CSK_{2.5}$ and 67.2% for CSK_{10}). In contrast, the best results for Sentinel-1 datasets were observed for AS combinations (68.8% and 66.9%, respectively). $RP^{\leq 500} \rightrightarrows MP$ and $RP^{>500} \rightrightarrows MP$ were not significantly influenced by the combinations of seasons but varied depending on the dataset. The lower and more favourable values, slightly higher than 1, were obtained for the $CSK_{2.5}$ dataset for $RP^{\leq 500} \rightrightarrows MP$, indicating that, on average, one reference patch overlapped with one mapped patch. For CSK_{10}, this value increased to approximately 1.4, and for Sentinel-1 datasets, it further increased to around 1.7. $RP^{>500} \rightrightarrows MP$ reached larger values (about 0.5 higher) keeping similar trends among sensors and season's combinations. $MP \rightrightarrows RP^{\leq 500}$ had very similar values for all sensors and combinations, with slightly higher values for $CSK_{2.5}$. Differently $MP \rightrightarrows RP^{>500}$ showed a clear difference between the results obtained with $CSK_{2.5}$ and the ones obtained with data at pixel spacing at 10 m: for $CSK_{2.5}$ the value of this metric was above 6, while for the other sensors it was around 1.8. It clearly indicated a high level of fragmentation for the $CSK_{2.5}$ results.

For the seasons combination that showed the highest accuracies (SS)

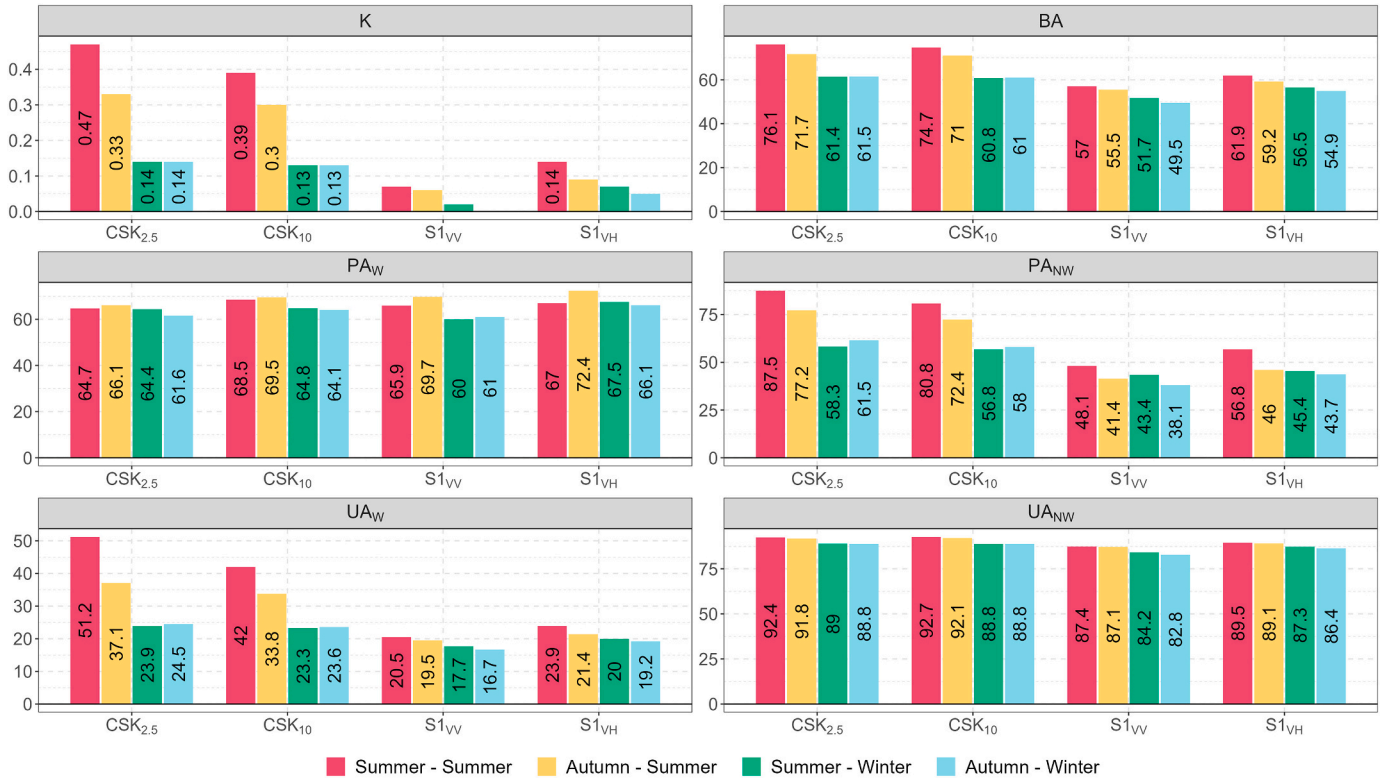

Fig. 6. Windthrows detection results at pixel level, different seasons and different spatial resolutions and sensors. The accuracy metrics are described in Table 3.

we provide in Table 4 also the results obtained considering the wall-to-wall coverage of the three areas (ascending plus descending data). These numbers confirm what showed in the figures considering only the areas after masking.

Fig. 8 and Fig. 9 illustrate the differences in the values of pixel and patch level accuracy metrics when considering all forest areas versus only evergreen areas. In the case of pixel level metrics, a negative value indicates an improvement when considering only evergreen areas, while a positive value indicates the opposite. For the COSMO-SkyMed combinations with a winter post-event image, all the pixel level metrics showed improvement when considering only evergreen areas. However, this improvement was not observed for the Sentinel-1 data, although the decrease in performance was limited. Notably, UA_{NW} consistently showed a decrease when considering only evergreen areas, particularly for the Sentinel-1 data. In terms of patch level metrics, when considering only evergreen areas, the average size of the patches (MP_{AREA}) increased (mainly for CSK_{10}, $S1_{VV}$ and $S1_{VH}$).

The distinctions between considering all forest areas and solely the evergreen areas are also evident in the detection maps presented in Fig. 10, Fig. 11, and Fig. 12. It is worth noting that a significant number of false alarms occurred in deciduous forest regions when utilizing winter post-event images (*SW* and *AW* season combinations) and when using Sentinel-1 data.

5. Discussion

To the best of our knowledge, this study represents the first investigation into the utilization of SAR COSMO-SkyMed data for detecting forest windthrows in mountainous regions, as well as the first comparative analysis with Sentinel-1 data. In summary, our analysis encompassed the following aspects: i) the effectiveness of different SAR data in X and C bands (COSMO-SkyMed and Sentinel-1, respectively) for windthrow detection; ii) the influence of varying pixel spacing in COSMO-SkyMed data and the utilization of different polarizations in Sentinel-1 data; iii) the impact of different combinations of seasonal imagery on windthrow detection; and iv) the implications of considering all tree species versus solely evergreen species. The outcomes of this study hold significant implications for the practical application of SAR data in windthrow detection and provide valuable insights for decision makers aiming to enhance forest management strategies.

5.1.1. Algorithm parameters setting

The proposed methodology requires tuning of only two parameters: i) the number of layers in the 2D-SWT, and ii) the thresholding direction for generating windthrow maps at each level. The number of 2D-SWT layers parameter should be set within a range of 3 to a value related to the image size. It is important to note that setting the number of layers too high may diminish the ability to detect small windthrow patches as the influence of higher layers increases. Previous studies by Bovolo and Bruzzone (2005) used a value of 8, while Marin et al. (2015) used $N = 4$. A suggestion is to adjust this value according to the spatial resolution of the images employed. In our preliminary experiments, we tested values of 3, 5, 7, and 9, and observed similar results for all values except for 3.

Regarding the second parameter, there are two options: considering as windthrows pixel values (i) above or (ii) below the Otsu threshold. In this study, we used values above the threshold for COSMO-SkyMed images and below the threshold for Sentinel-1 images. This choice was based on some initial analysis of the decomposed/reconstructed images, where we observed an increase in values within windthrow areas for COSMO-SkyMed data and a decrease for Sentinel-1 data. Further analysing the literature, we found some previous studies supporting this choice. Eriksson et al. (2012) investigated the backscatter values of forest windthrows across different SAR bands and found that the backscatter signal from TerraSAR-X (X-band) increased by approximately 1.5 dB for fallen trees compared to standing trees, while ALOS PALSAR (L-band) showed a decrease of the same magnitude. Tomppo et al. (2021) mapped forest windthrows using Sentinel-1 data (C-band) and

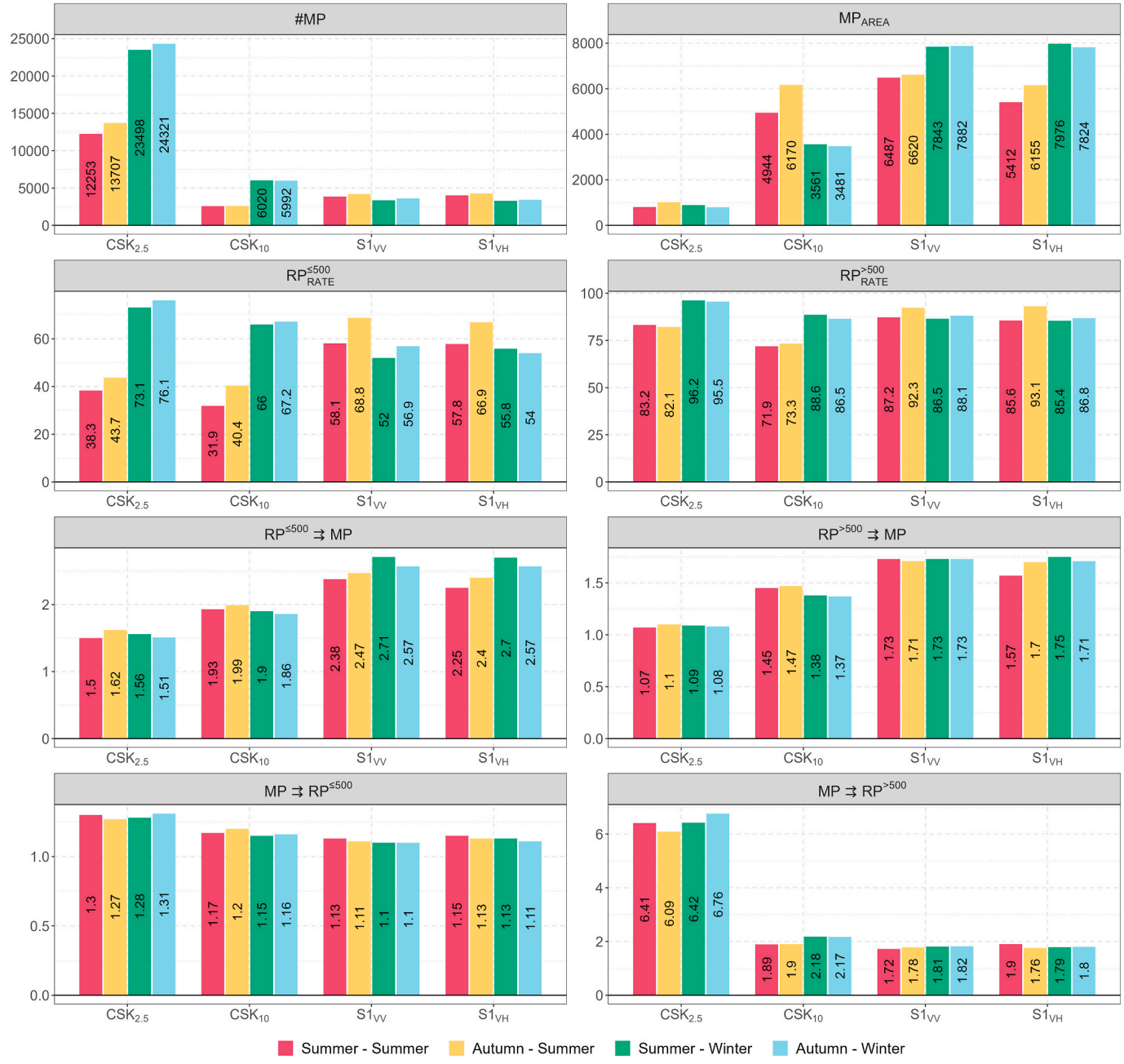

Fig. 7. Windthrows detection results at patch level, different seasons and different spatial resolutions and sensors. The accuracy metrics are described in Table 3.

noted that extensive and severe windstorm damage may cause a decrease in backscatter intensity similar to clear-cut areas, whereas small-scale damage can lead to an increase in backscatter in neighbouring areas due to various scattering mechanisms.

Indeed, some information about the location of the windthrow event could enhance the results. This does not imply the need for extensive field observations, but rather that some preliminary information could be advantageous. Typically, such information is available when applying a detection method, as it assumes knowledge of a windthrow event having occurred.

5.1.2. Capability to detect forest windthrows using SAR data in C and X bands in mountain areas

In mountainous areas, the use of remote sensing data, including both SAR and optical images, for windthrow detection is influenced by two primary factors: morphology and weather conditions. With respect to morphology, both SAR and optical images face challenges due to the complex terrain found in mountain regions. In SAR data, this complexity results in layover and shadow areas that are not suitable for windthrow detection. While using images acquired in a single orbit direction (ascending or descending) enables windthrow detection, the presence of extensive layover and shadow areas in mountainous regions compromises the mapping of all damages. To ensure the practical application of SAR data for windthrow detection, it is crucial to have access to images acquired from both viewing geometries. Unlike Sentinel-1 data, which provides continuous image acquisitions, COSMO-SkyMed data is acquired on-demand. This limitation is inherent to all on-demand systems and should be considered when making use of such data. Since windthrow events cannot be predicted in advance, the availability of both ascending and descending images would likely be limited to the post-event period. This potential limitation may impact the use of COSMO-SkyMed data with the adopted methodology, particularly outside of

Table 4
Accuracy metrics obtained for the four scenarios in the case of SS seasons combinations combining all the three areas and ascending and descending data.

	$CSK_{2.5}$	CSK_{10}	$S1_{VV}$	$S1_{VH}$
K	0.46	0.39	0.09	0.14
BA	75.2	73.8	59.4	63.6
PA_W	61.5	64.5	73.1	72.9
PA_{NW}	88.8	83	45.6	54.3
UA_W	50.2	41.1	19.8	22.6
UA_{NW}	92.6	92.7	90.2	91.6
$\#MP$	16,082	3072	3153	3210
MP_{AREA}	831	5583	13,172	11,166
$RP_{DET}^{\leq 500}$	42.8	35.8	71.1	66.2
$RP_{DET}^{>500}$	81.8	71.9	93	90.3
$MP \rightrightarrows RP^{\leq 500}$	1.66	2.49	7.24	4.99
$MP \rightrightarrows RP^{>500}$	1.16	1.01	1.01	1.02
$RP^{\leq 500} \rightrightarrows MP$	1.07	1.47	2.38	2.15
$RP^{>500} \rightrightarrows MP$	7.07	1.88	1.56	1.6

Italy, as Italy benefits from a relatively large archive of past COSMO-SkyMed acquisitions. Regarding the combination of ascending and descending data, this study employed a combination of windthrow maps generated from both data sources. More advanced methods for combining these data involve creating composites prior to applying the windthrow detection method. Several studies have investigated the optimal procedures for this composite creation (Rüetschi et al., 2019; Small et al., 2022).

While SAR data is generally less affected by clouds and precipitation compared to optical data, they can still be impacted. Danklmayer et al. (2009) demonstrated that heavy precipitations events cause artifacts in X-band SAR images. Conversely, C-band data is less susceptible to precipitations, although a heavy precipitations event can cause attenuation of the SAR signal. The effects of precipitations can persist for hours after the event due to the high humidity in the air and on the ground. In our study, as depicted in Fig. 2, we carefully selected images that were not acquired during or immediately after heavy precipitations events. This ensures that the analyses presented in this study are not influenced by adverse precipitations conditions. It is important to consider this factor when choosing SAR images, especially in mountainous regions that are prone to heavy precipitations.

The disparities in results between COSMO-SkyMed data and Sentinel-1 data are substantial, with COSMO-SkyMed consistently outperforming Sentinel-1 and yielding significantly better outcomes. Both at the pixel and patch levels, Sentinel-1 produced a higher number of false alarms. This is evident from the low values of PA_{NW} and UA_W at the pixel level, as well as the high $RP \rightrightarrows MP$ metric (approximately 2.5). Sentinel-1 tends to detect very large windthrow patches, which inflates PA_W, $RP_{DET}^{\leq 500}$ and $RP_{DET}^{>500}$ at the expense of numerous false alarms. These findings suggest that the proposed methodology is better suited for detecting forest windthrows using COSMO-SkyMed data. While Tomppo et al. (2021) emphasized the challenges of windthrow detection using C-band data, there are existing studies in the literature that employed Sentinel-1 data for analysing different forest disturbances such as windthrows, droughts or ice related affectations (Lazecky et al., 2021; Rüetschi et al., 2019; Schellenberg et al., 2023; Zoltán et al., 2021). Regarding windthrows, Rüetschi et al. (2019) reported, a producer's accuracy of 88% and user's accuracy of 85%, while Lazecky et al. (2021) did not provided results in terms of accuracies. For other type of disturbances, overall accuracies of 65.7% are reported (Zoltán et al., 2021). This may imply that the results are dependent on the specific algorithm employed, and therefore, the adopted methodology may not be ideal for analysing Sentinel-1 data.

5.1.3. *Impacts of using different pixel spacing: pixel vs patch-level analysis*

The choice of pixel spacing for generating the sigma0 band from level 1B data appears to have some impact on the results. In this study, we considered pixel spacings of 2.5 m and 10 m for the COSMO-SkyMed data. It is important to note that both pixel spacings are high and capable of capturing small windthrow patches. Examining the pixel-

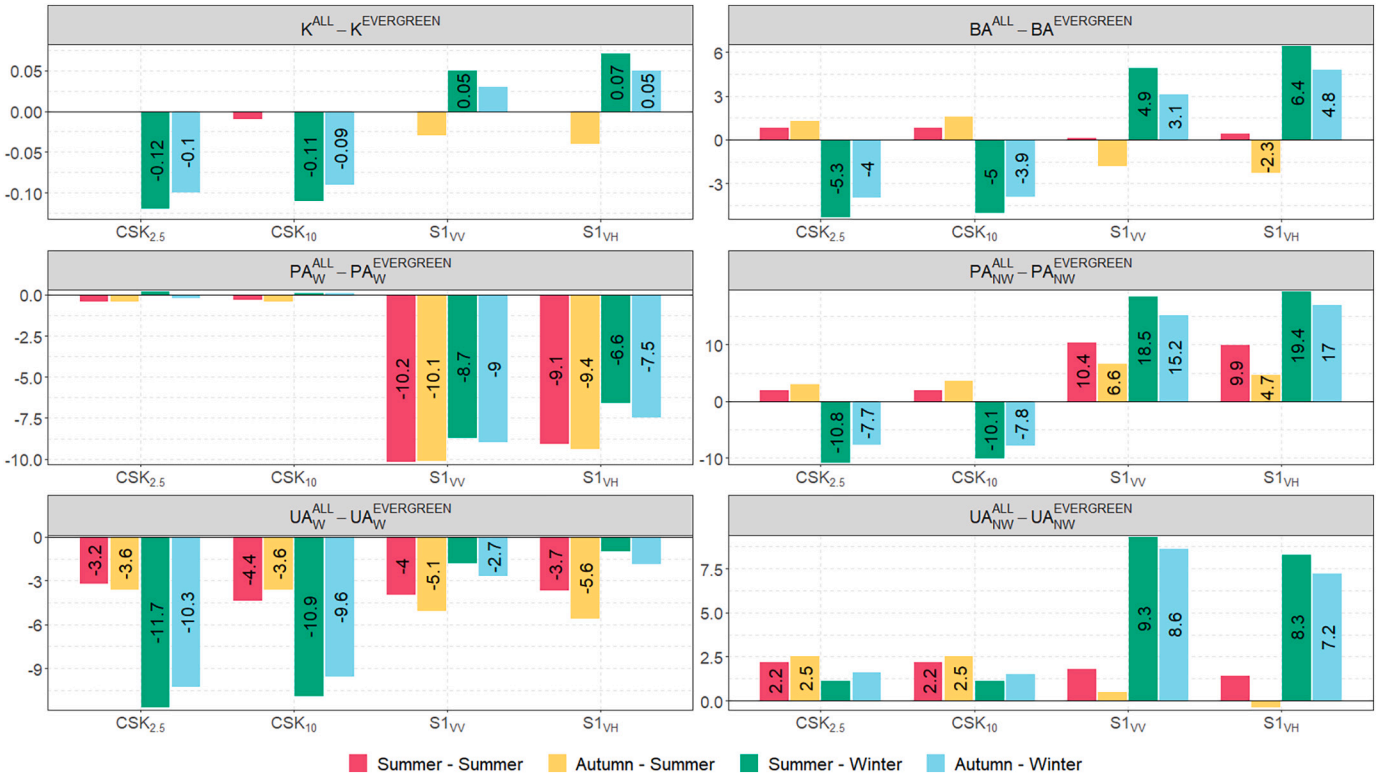

Fig. 8. Differences of the pixel level accuracy metrics (see Table 3) between all pixels (superscript ALL) and pixels over evergreen forest areas (superscript EVERGREEN).

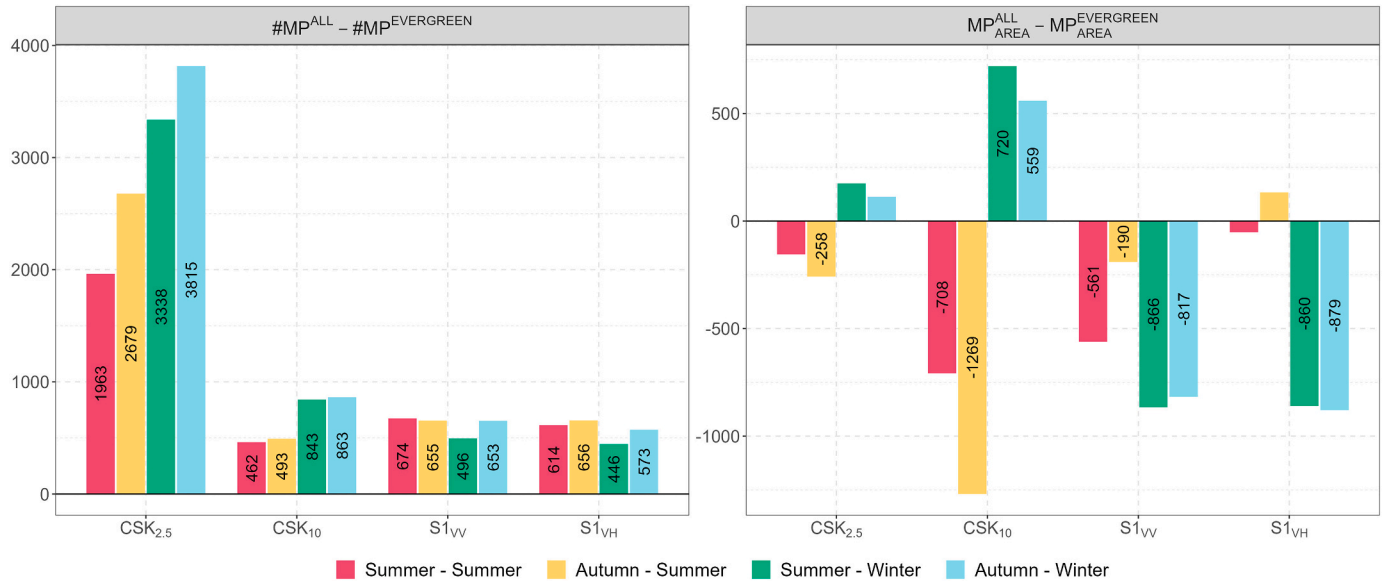

Fig. 9. Differences of patch level accuracy metrics (see Table 3) between all patches (superscript ALL) and patches containing only evergreen forest (superscript EVERGREEN).

level accuracies in Fig. 6, we observed slightly better results for the $CSK_{2.5}$ case, while using CSK_{10} data resulted in a slight decrease (2–7%) in PA_{NW} compared to $CSK_{2.5}$, indicating a higher number of false alarms with 10 m data. This trend is also evident in the patch-level results shown in Fig. 7, where using a 10 m spatial resolution led to an increase in MP_{AREA}, $RP^{\leq 500} \rightrightarrows MP$ and $RP^{>500} \rightrightarrows MP$ metrics. The $RP^{\leq 500} \rightrightarrows MP$ metric indicated that, on average, there were approximately 2 or more reference patches per mapped patch when using a 10 m spatial resolution. Conversely, employing a 2.5 m spatial resolution resulted in a significant increase in the number of windthrow patches ($\#MP$) and $MP \rightrightarrows RP^{>500}$, indicating that reference patches were split into multiple patches. In this study, we did not apply any post-processing to the output maps of the windthrow detection algorithm to provide a simple methodology. However, post-processing techniques such as majority filtering or removing very small patches (e.g., those consisting of only 1 or 2 pixels in the $CSK_{2.5}$ data) could marginally improve the results, especially at the patch level. Such post-processing steps are particularly relevant for $CSK_{2.5}$ maps, where single-pixel windthrow detections are more likely to be noise than genuine detections. Nevertheless, based on the presented results, we can conclude that a high spatial resolution (2.5 m pixel spacing) is advantageous, although working with data at 10 m spatial resolution is more practical and enables faster processing over large areas. It is important to note that these considerations are specific to the analysed event in this study, where the median patch size (472.5 m^2 for area A, 288 m^2 for area B, and 567 m^2 for area C) was much larger than 100 m^2 (the size of a 10 × 10 pixel). In other scenarios, where trees are smaller (e.g., boreal forests), degrading the resolution could have a more significant impact on the results.

Regarding Sentinel-1 data, both VV and VH polarizations were analysed over the study areas. The results were quite similar between the two polarizations, although VH polarization exhibited slightly better performance. This observation aligns with previous studies in the literature (Rüetschi et al., 2019; Schellenberg et al., 2023; Zoltán et al., 2021). Rüetschi et al. (2017) suggested that this behaviour could be attributed to the changing scattering mechanisms when the wooded material is randomly oriented after windthrow, making cross-polarized backscatter (VH) more sensitive to this random arrangement of scatterers compared to co-polarized channels (VV).

5.1.4. Influence of different seasons' combinations

The choice of seasons' combinations was found to be a crucial factor in achieving accurate windthrow detections, regardless of the data source (COSMO-SkyMed or Sentinel-1), pixel spacing (2.5 m and 10 m), and polarization. The use of a summer post-event image consistently outperformed a winter post-event image. The pre-event image had a lesser impact on the accuracy, although having a summer pre-event image also improved the results. These findings are specific to the algorithm used, the analysed event (which occurred in late autumn), and the characteristics of the forests (including both deciduous and evergreen species). However, these characteristics provided valuable insights into windthrow detection. Combining pre and post-event images acquired when the forest was in the same phenological phase was crucial for eliminating false alarms related to forest phenology. It is important to note that achieving such temporal alignment may not always be feasible, especially if the event occurs in autumn or winter when rapid detection is required after the event.

Alternatively, heterogeneous change detection using both SAR and optical data or relying on a single post-event image are potential approaches. In the case of heterogeneous change detection, several studies in the literature address complex detections of this nature (Chen et al., 2022, 2023; Jiang et al., 2020; Sun et al., 2022). However, using a single post-event image would shift the analysis from a change detection scenario to a land cover classification task. In such cases, additional research would be needed to collect windthrow reference data for supervised classification or to select an appropriate unsupervised approach and detection features. Therefore, using pre- and post-event data with similar seasonality could serve as an alternative solution that remains unsupervised, avoiding the need for additional reference data collection or a complex classification framework.

5.1.5. Implications of different forest types

In this study, it was demonstrated that having prior knowledge about the area, particularly regarding the dominant tree species, can significantly improve the results even under non-optimal conditions. In the case of the analysed Vaia storm, where the majority of the damage occurred in Norway spruce forests, using a forest management plan layer to filter the data and focus on evergreen stands resulted in a substantial reduction in false alarms, especially in the autumn/winter combination. This improvement was evident at both the pixel and patch level analyses. At the pixel level, there was an enhancement in all metrics, particularly in terms of the user's accuracy for windthrow detection, indicating a significant reduction in false alarms. At the patch level, the

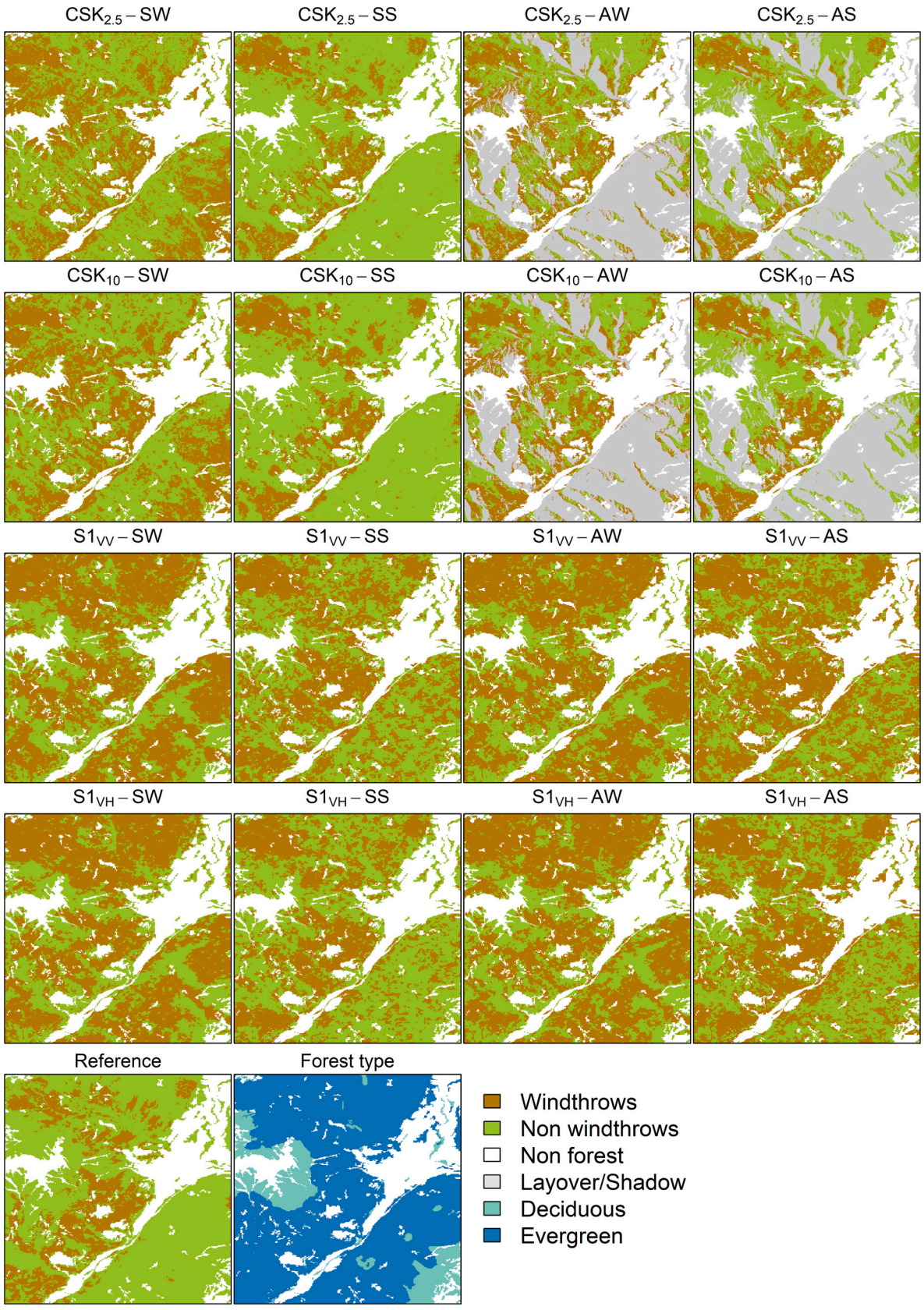

Fig. 10. Windthrows detection maps for the study area A.

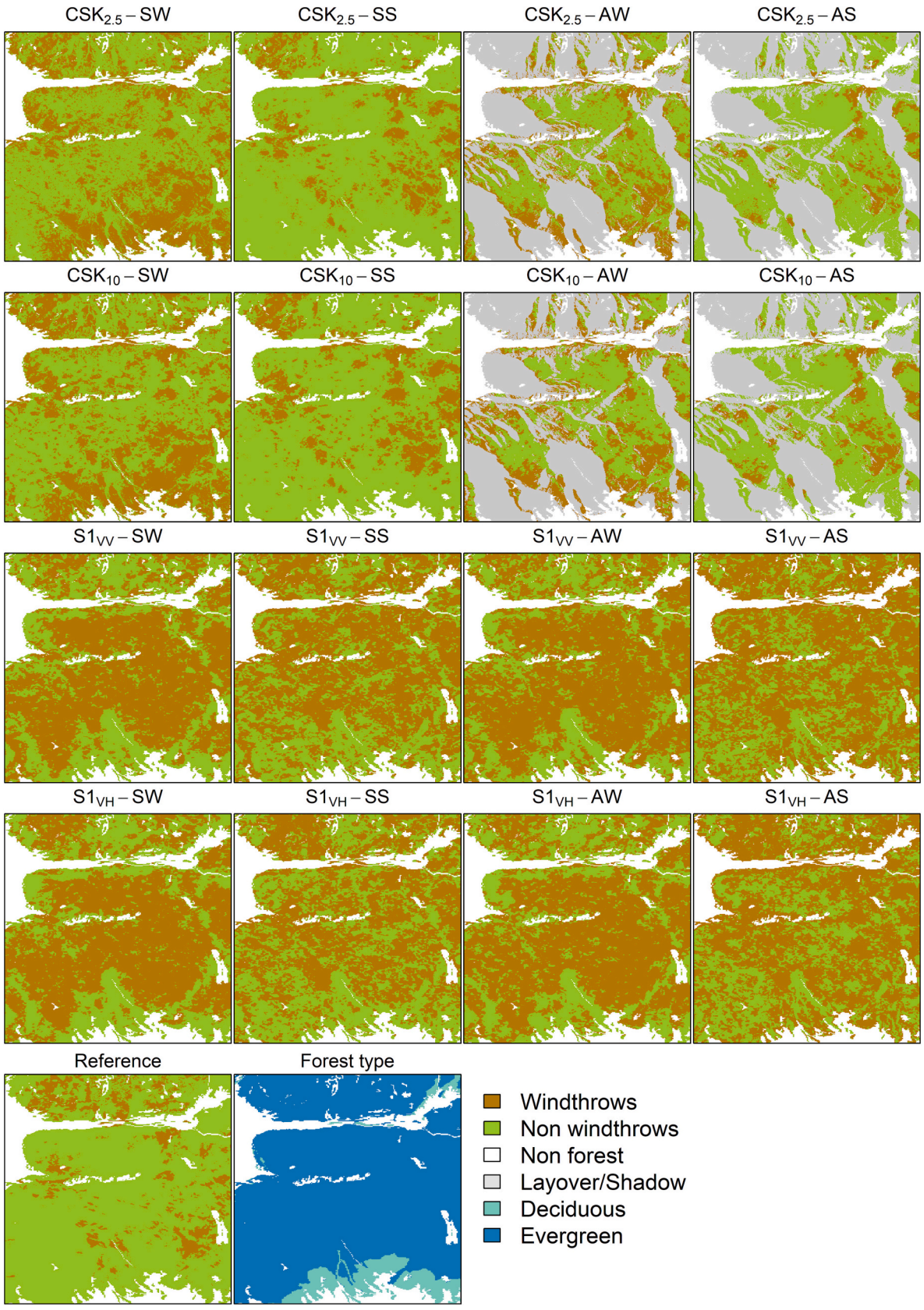

Fig. 11. Windthrows detection maps for the study area B.

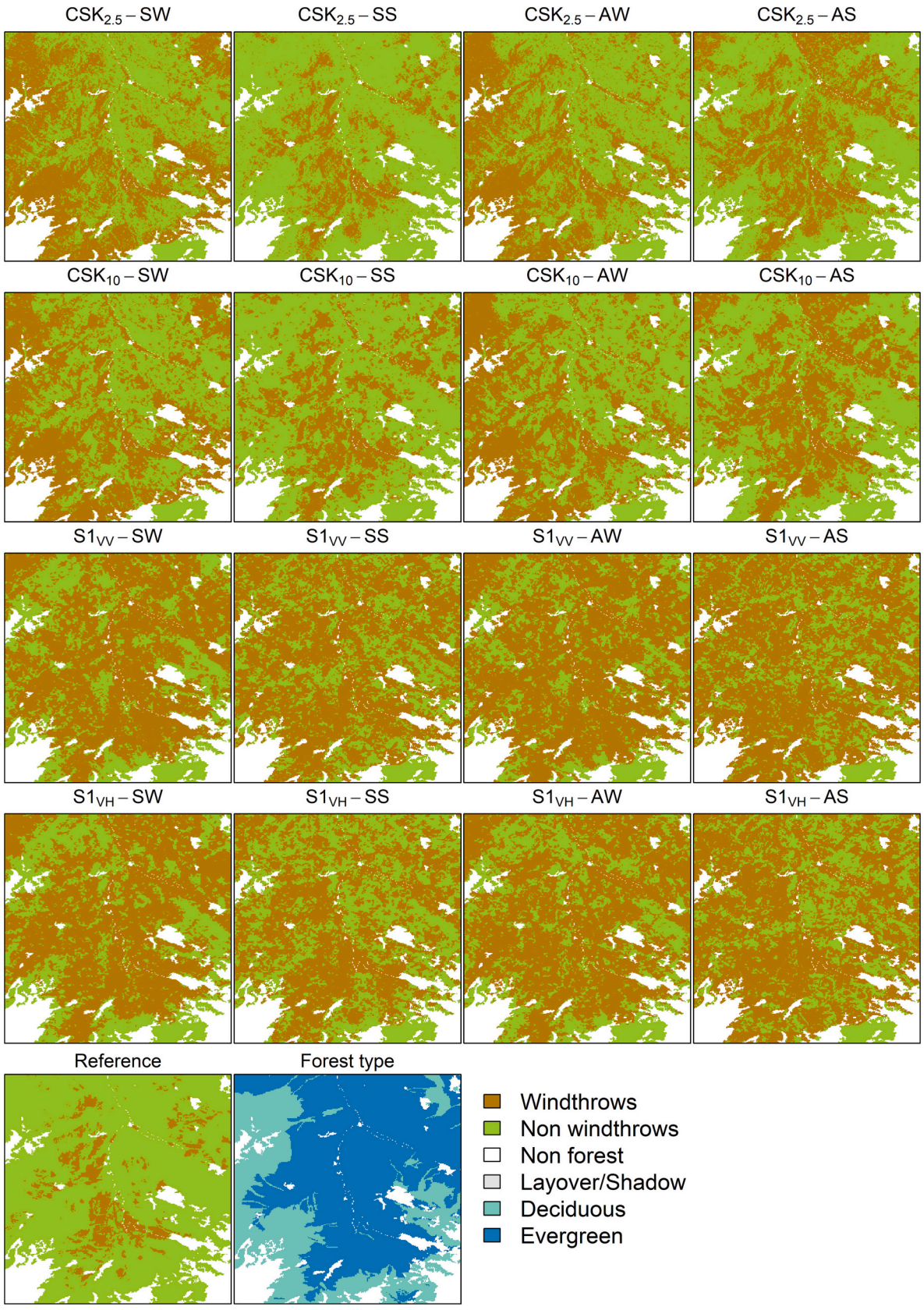

Fig. 12. Windthrows detection maps for the study area C.

analysis showed a decrease in the number of windthrow patches (#*MP*) and an increase in the average patch area (MP_{AREA}), further confirming the effectiveness of masking based on forest type. However, in cases where prior knowledge about the forest type is not available, or if the windthrow event affects both evergreen and deciduous forests, alternative algorithms should be employed. These algorithms should be capable of detecting multiple types of changes, such as Change Vector Analysis (CVA) or multiscale convolutional networks (He et al., 2021; Lv et al., 2022; Solano-Correa et al., 2019; Tang et al., 2022). Additionally, distinguishing different tree species using optical data and a supervised classification approach could also be employed (Udali et al., 2021). These methods can overcome the limitations posed by lacking prior knowledge of the forest type or dealing with mixed forest stands affected by windthrows.

6. Conclusions

The presented study focused on the detection of forest windthrows in mountain areas using COSMO-SkyMed (band X) and Sentinel-1 SAR (band C) data. At the best of our knowledge this is the first study to analyse COSMO-SkyMed data for windthrows detection. A multiscale decomposition/reconstruction strategy was employed, and various combinations of data were investigated, including different pixel spacings (2.5 m and 10 m), images acquired at different times before and after the windthrow event, and different forest types. The comparisons conducted in this study demonstrated that COSMO-SkyMed outperformed Sentinel-1 for windthrows detection using the adopted methodology. It was observed that combining images acquired under optimal conditions, such as during the summer season in this study, yielded the best results and minimized false alarms. The phenology of trees, specifically the transition between leaf-on and leaf-off conditions, was found to have a significant impact on windthrow detection results. The pixel spacing was also identified as a contributing factor, although the difference in performance between COSMO-SkyMed at 2.5 m and 10 m pixel spacing was relatively small. However, further exploration of change detection techniques capable of detecting multiple changes could be beneficial in reducing false alarms resulting from phenological changes in broadleaf species.

Declaration of generative AI and AI-assisted technologies in the writing process

During the preparation of this work the authors used ChatGPT in order to improve the English language. After using this tool/service, the authors reviewed and edited the content as needed and takes full responsibility for the content of the publication.

Authors contribution

Michele Dalponte: Conceptualization, Methodology, Software, Validation, Formal analysis, Investigation, Resources, Writing - Original Draft, Writing - Review & Editing, Visualization. **Yady Tatiana Solano-Correa**: Conceptualization, Methodology, Validation, Investigation, Writing - Original Draft, Writing - Review & Editing. **Daniele Marinelli**: Conceptualization, Methodology, Validation, Investigation, Writing - Original Draft, Writing - Review & Editing. **Sicong Liu**: Validation, Writing - Review & Editing. **Naoto Yokoya**: Resources, Writing - Review & Editing. **Damiano Gianelle**: Writing - Review & Editing, Supervision, Funding acquisition.

Declaration of Competing Interest

The authors declare that they have no known competing financial interests or personal relationships that could have appeared to influence the work reported in this paper.

Data availability

The authors do not have permission to share data.

Acknowledgements

This work was carried out using CSK® Products, © ASI (Italian Space Agency), delivered under an ASI licence to use. The authors would like to thank Planet Labs, Inc. for providing access to their daily imagery through the education and research program. This work was funded by the Highlander project co-financed by the Connecting European Facility Programme of the European Union Grant agreement n° INEA/CEF/ICT/A2018/1815462.

Appendix A. Supplementary data

Supplementary data to this article can be found online at https://doi.org/10.1016/j.rse.2023.113787.

References

Abdikan, S., Bayik, C., Sekertekin, A., Bektas Balcik, F., Karimzadeh, S., Matsuoka, M., Balik Sanli, F., 2022. Burned area detection using multi-sensor SAR, optical, and thermal data in Mediterranean pine forest. Forests 13, 347. https://doi.org/10.3390/f13020347.

Albrecht, A., Hanewinkel, M., Bauhus, J., Kohnle, U., 2012. How does silviculture affect storm damage in forests of South-Western Germany? Results from empirical modeling based on long-term observations. Eur. J. For. Res. 131, 229–247. https://doi.org/10.1007/s10342-010-0432-x.

Ban, Y., Zhang, P., Nascetti, A., Bevington, A.R., Wulder, M.A., 2020. Near real-time wildfire progression monitoring with Sentinel-1 SAR time series and deep learning. Sci. Rep. 10, 1322. https://doi.org/10.1038/s41598-019-56967-x.

Belenguer-Plomer, M.A., Tanase, M.A., Chuvieco, E., Bovolo, F., 2021. CNN-based burned area mapping using radar and optical data. Remote Sens. Environ. 260, 112468 https://doi.org/10.1016/j.rse.2021.112468.

Bernardi, M.S., Africa, P.C., de Falco, C., Formaggia, L., Menafoglio, A., Vantini, S., 2021. On the use of interferometric synthetic aperture radar data for monitoring and forecasting natural hazards. Math. Geosci. 53, 1781–1812. https://doi.org/10.1007/s11004-021-09948-8.

Bovolo, F., Bruzzone, L., 2005. A detail-preserving scale-driven approach to change detection in multitemporal SAR images. IEEE Trans. Geosci. Remote Sens. 43, 2963–2972. https://doi.org/10.1109/TGRS.2005.857987.

Chen, H., Yokoya, N., Chini, M., 2023. Fourier domain structural relationship analysis for unsupervised multimodal change detection. ISPRS J. Photogramm. Remote Sens. 198, 99–114. https://doi.org/10.1016/j.isprsjprs.2023.03.004.

Chen, H., Yokoya, N., Wu, C., Du, B., 2022. Unsupervised multimodal change detection based on structural relationship graph representation learning. IEEE Trans. Geosci. Remote Sensing 60, 1–18. https://doi.org/10.1109/TGRS.2022.3229027.

Chen, X., Sun, Q., Hu, J., 2018. Generation of complete SAR geometric distortion maps based on DEM and neighbor gradient algorithm. Appl. Sci. 8, 2206. https://doi.org/10.3390/app8112206.

Chirici, G., Giannetti, F., Travaglini, D., Nocentini, S., Francini, S., D'Amico, G., Calvo, E., Fasolini, D., Broll, M., Maistrelli, F., Tonner, J., Pietrogiovanna, M., Oberlechner, K., Andriolo, A., Comino, R., Faidiga, A., Pasutto, I., Carraro, G., Zen, S., Contarin, F., Alfonsi, L., Wolynski, A., Zanin, M., Gagliano, C., Tonolli, S., Zoanetti, R., Tonetti, R., Cavalli, R., Lingua, E., Pirotti, F., Grigolato, S., Bellingeri, D., Zini, E., Gianelle, D., Dalponte, M., Pompei, E., Stefani, A., Motta, R., Morresi, D., Garbarino, M., Alberti, G., Valdevit, F., Tomelleri, E., Torresani, M., Tonon, G., Marchi, M., Corona, P., Marchetti, M., 2019. In: Forest damage inventory after the "Vaia" storm in Italy. Forest@ - Rivista di Selvicoltura ed Ecologia Forestale 16, pp. 3–9. https://doi.org/10.3832/efor3070-016.

Cigna, F., Bateson, L.B., Jordan, C.J., Dashwood, C., 2014. Simulating SAR geometric distortions and predicting persistent scatterer densities for ERS-1/2 and ENVISAT C-band SAR and InSAR applications: Nationwide feasibility assessment to monitor the landmass of Great Britain with SAR imagery. Remote Sens. Environ. 152, 441–466. https://doi.org/10.1016/j.rse.2014.06.025.

Dalponte, M., Marzini, S., Solano-Correa, Y.T., Tonon, G., Vescovo, L., Gianelle, D., 2020. Mapping forest windthrows using high spatial resolution multispectral satellite images. Int. J. Appl. Earth Obs. Geoinf. 93, 102206 https://doi.org/10.1016/j.jag.2020.102206.

Danklmayer, A., Doring, B.J., Schwerdt, M., Chandra, M., 2009. Assessment of atmospheric propagation effects in SAR images. IEEE Trans. Geosci. Remote Sens. 47, 3507–3518. https://doi.org/10.1109/TGRS.2009.2022271.

Deigele, W., Brandmeier, M., Straub, C., 2020. A hierarchical deep-learning approach for rapid windthrow detection on PlanetScope and high-resolution aerial image data. Remote Sens. 12, 2121. https://doi.org/10.3390/rs12132121.

Duan, F., Wan, Y., Deng, L., 2017. A novel approach for coarse-to-fine windthrown tree extraction based on unmanned aerial vehicle images. Remote Sens. 9, 306. https://doi.org/10.3390/rs9040306.

Einzmann, K., Immitzer, M., Böck, S., Bauer, O., Schmitt, A., Atzberger, C., 2017. Windthrow detection in european forests with very high-resolution optical data. Forests 8, 21. https://doi.org/10.3390/f8010021.

Eriksson, L.E.B., Fransson, J.E.S., Soja, M.J., Santoro, M., 2012. Backscatter signatures of wind-thrown forest in satellite SAR images. In: 2012 IEEE International Geoscience and Remote Sensing Symposium. Presented at the IGARSS 2012 - 2012 IEEE International Geoscience and Remote Sensing Symposium, IEEE, Munich, Germany, pp. 6435–6438. https://doi.org/10.1109/IGARSS.2012.6352732.

Fransson, J.E.S., Walter, F., Blennow, K., Gustavsson, A., Ulander, L.M.H., 2002. Detection of storm-damaged forested areas using airborne CARABAS-II VHF SAR image data. IEEE Trans. Geosci. Remote Sens. 40, 2170–2175. https://doi.org/10.1109/TGRS.2002.804913.

Giovannini, L., Davolio, S., Zaramella, M., Zardi, D., Borga, M., 2021. Multi-model convection-resolving simulations of the october 2018 vaia storm over northeastern Italy. Atmos. Res. 253, 105455 https://doi.org/10.1016/j.atmosres.2021.105455.

Green, R.M., 1998. The sensitivity of SAR backscatter to forest windthrow gaps. Int. J. Remote Sens. 19, 2419–2425. https://doi.org/10.1080/014311698214811.

Hamdi, Z.M., Brandmeier, M., Straub, C., 2019. Forest damage assessment using deep learning on high resolution remote sensing data. Remote Sens. 11, 1976. https://doi.org/10.3390/rs11171976.

He, P., Zhao, X., Shi, Y., Cai, L., 2021. Unsupervised change detection from remotely sensed images based on multi-scale visual saliency coarse-to-fine fusion. Remote Sens. 13, 630. https://doi.org/10.3390/rs13040630.

Horch, A., Djemal, K., Gafour, A., Taleb, N., 2019. Supervised fusion approach of local features extracted from SAR images for detecting deforestation changes. IET Image Process. 13, 2866–2876. https://doi.org/10.1049/iet-ipr.2019.0122.

Hosseini, M., Lim, S., 2023. Burned area detection using Sentinel-1 SAR data: A case study of Kangaroo Island, South Australia. Appl. Geogr 151, 102854. https://doi.org/10.1016/j.apgeog.2022.102854.

Italian Space Agency, 2019. COSMO-SkyMed Mission and Products Description.

Jalkanen, A., Mattila, U., 2000. Logistic regression models for wind and snow damage in northern Finland based on the National Forest Inventory data. For. Ecol. Manag. 135, 315–330. https://doi.org/10.1016/S0378-1127(00)00289-9.

Jiang, X., Li, G., Liu, Y., Zhang, X.-P., He, Y., 2020. Change detection in heterogeneous optical and SAR remote sensing images via deep homogeneous feature fusion. IEEE J. Sel. Top. Appl. Earth Observations Remote Sensing 13, 1551–1566. https://doi.org/10.1109/JSTARS.2020.2983993.

Jonikavičius, D., Mozgeris, G., 2013. Rapid assessment of wind storm-caused forest damage using satellite images and stand-wise forest inventory data. iForest -. Biogeosci. Forestry 6, 150–155. https://doi.org/10.3832/ifor0715-006.

Kellndorfer, J.M., Pierce, L.E., Dobson, M.C., Ulaby, F.T., 1998. Toward consistent regional-to-global-scale vegetation characterization using orbital SAR systems. IEEE Trans. Geosci. Remote Sens. 36, 1396–1411. https://doi.org/10.1109/36.718844.

Kislov, D.E., Korznikov, K.A., 2020. Automatic windthrow detection using very-high-resolution satellite imagery and deep learning. Remote Sens. 12, 1145. https://doi.org/10.3390/rs12071145.

Lazecky, M., Wadhwa, S., Mlcousek, M., Sousa, J.J., 2021. Simple method for identification of forest windthrows from Sentinel-1 SAR data incorporating PCA. Proc. Computer Sci. 181, 1154–1161. https://doi.org/10.1016/j.procs.2021.01.312.

Lv, Z., Liu, T., Benediktsson, J.A., Falco, N., 2022. Land cover change detection techniques: very-high-resolution optical images: a review. IEEE Geosci. Remote Sens. Mag. 10, 44–63. https://doi.org/10.1109/MGRS.2021.3088865.

Marin, C., Bovolo, F., Bruzzone, L., 2015. Building change detection in multitemporal very high resolution SAR images. IEEE Trans. Geosci. Remote Sens. 53, 2664–2682. https://doi.org/10.1109/TGRS.2014.2363548.

Mitchell, S.J., 2013. Wind as a natural disturbance agent in forests: a synthesis. Forestry 86, 147–157. https://doi.org/10.1093/forestry/cps058.

Nyström, M., Holmgren, J., Fransson, J.E.S., Olsson, H., 2014. Detection of windthrown trees using airborne laser scanning. Int. J. Appl. Earth Obs. Geoinf. 30, 21–29. https://doi.org/10.1016/j.jag.2014.01.012.

Otsu, N., 1979. A threshold selection method from gray-level histograms. IEEE Trans. Syst., Man, Cybern. 9, 62–66. https://doi.org/10.1109/TSMC.1979.4310076.

Patacca, M., Lindner, M., Lucas-Borja, M.E., Cordonnier, T., Fidej, G., Gardiner, B., Hauf, Y., Jasinevičius, G., Labonne, S., Linkevičius, E., Mahnken, M., Milanovic, S., Nabuurs, G., Nagel, T.A., Nikinmaa, L., Panyatov, M., Bercak, R., Seidl, R., Ostrogović Sever, M.Z., Socha, J., Thom, D., Vuletic, D., Zudin, S., Schelhaas, M., 2023. Significant increase in natural disturbance impacts on European forests since 1950. Global Change Biology 29, 1359–1376. https://doi.org/10.1111/gcb.16531.

Pirotti, F., Travaglini, D., Giannetti, F., Kutchartt, E., Bottalico, F., Chirici, G., 2016. In: Kernel feature cross-correlation for unsupervised quantification of damage from windthrow in forests. ISPRS - International Archives of the Photogrammetry, Remote Sensing and Spatial Information Sciences XLI-B7, pp. 17–22. https://doi.org/10.5194/isprs-archives-XLI-B7-17-2016.

Quine, C.P., Gardiner, B.A., Moore, J., 2021. Wind disturbance in forests: The process of wind created gaps, tree overturning, and stem breakage. In: Plant Disturbance Ecology. Elsevier, pp. 117–184. https://doi.org/10.1016/B978-0-12-818813-2.00004-6.

Rich, R.L., Frelich, L., Reich, P.B., Bauer, M.E., 2010. Detecting wind disturbance severity and canopy heterogeneity in boreal forest by coupling high-spatial resolution satellite imagery and field data. Remote Sens. Environ. 114, 299–308. https://doi.org/10.1016/j.rse.2009.09.005.

Rüetschi, M., Schaepman, M., Small, D., 2017. Using multitemporal Sentinel-1 C-band backscatter to monitor phenology and classify deciduous and coniferous forests in northern Switzerland. Remote Sens. 10, 55. https://doi.org/10.3390/rs10010055.

Rüetschi, M., Small, D., Waser, L., 2019. Rapid detection of windthrows using Sentinel-1 C-band SAR data. Remote Sens. 11, 115. https://doi.org/10.3390/rs11020115.

Sanginés de Cárcer, P., Mederski, P.S., Magagnotti, N., Spinelli, R., Engler, B., Seidl, R., Eriksson, A., Eggers, J., Bont, L.G., Schweier, J., 2021. The management response to wind disturbances in european forests. Curr Forestry Rep 7, 167–180. https://doi.org/10.1007/s40725-021-00144-9.

Schelhaas, M.-J., 2008. Impacts of natural disturbances on the development of european forest resources: application of model approaches from tree and stand levels to large-scale scenarios. Dissertationes Forestales 2008. https://doi.org/10.14214/df.56.

Schellenberg, K., Jagdhuber, T., Zehner, M., Hese, S., Urban, M., Urbazaev, M., Hartmann, H., Schmullius, C., Dubois, C., 2023. Potential of Sentinel-1 SAR to assess damage in drought-affected temperate deciduous broadleaf forests. Remote Sens. 15, 1004. https://doi.org/10.3390/rs15041004.

Schwarz, M., Steinmeier, C., Holecz, F., Stebler, O., Wagner, H., 2003. Detection of windthrow in mountainous regions with different remote sensing data and classification methods. Scand. J. For. Res. 18, 525–536. https://doi.org/10.1080/02827580310018023.

Seidl, R., Schelhaas, M.-J., Rammer, W., Verkerk, P.J., 2014. Increasing forest disturbances in Europe and their impact on carbon storage. Nat. Clim. Chang. 4, 806–810. https://doi.org/10.1038/nclimate2318.

Servizio Foreste e Fauna - Provincia Autonoma di Trento, 2018. Stato d'attuazione del Piano d'azione per la gestione degli interventi di esbosco e ricostruzione dei boschi danneggiati dagli eventi eccezionali nei giorni dal 27 al 30 ottobre 2018 - 1° report 2018. Trento, Italy.

Small, D., Rohner, C., Miranda, N., Ruetschi, M., Schaepman, M.E., 2022. Wide-area analysis-ready radar backscatter composites. IEEE Trans. Geosci. Remote Sens. 60, 1–14. https://doi.org/10.1109/TGRS.2021.3055562.

Small, D., Schuber, A., 2008. Guide to ASAR Geocoding.

Solano-Correa, Y.T., Bovolo, F., Bruzzone, L., 2019. An approach to multiple change detection in VHR optical images based on iterative clustering and adaptive thresholding. IEEE Geosci. Remote Sens. Lett. 16, 1334–1338. https://doi.org/10.1109/LGRS.2019.2896385.

Sun, Y., Lei, L., Guan, D., Kuang, G., Liu, L., 2022. Graph signal processing for heterogeneous change detection. IEEE Trans. Geosci. Remote Sens. 60, 1–23. https://doi.org/10.1109/TGRS.2022.3221489.

Tanase, M.A., Aponte, C., Mermoz, S., Bouvet, A., Le Toan, T., Heurich, M., 2018. Detection of windthrows and insect outbreaks by L-band SAR: a case study in the bavarian Forest National Park. Remote Sens. Environ. 209, 700–711. https://doi.org/10.1016/j.rse.2018.03.009.

Tang, X., Zhang, H., Mou, L., Liu, F., Zhang, X., Zhu, X.X., Jiao, L., 2022. An unsupervised remote sensing change detection method based on multiscale graph convolutional network and metric learning. IEEE Trans. Geosci. Remote Sensing 60, 1–15. https://doi.org/10.1109/TGRS.2021.3106381.

Thiele, A., Boldt, M., Hinz, S., 2012. Automated detection of storm damage in forest areas by analyzing TerraSAR-X data. In: 2012 IEEE International Geoscience and Remote Sensing Symposium. Presented at the IGARSS 2012 - 2012 IEEE International Geoscience and Remote Sensing Symposium, IEEE, Munich, Germany, pp. 1672–1675. https://doi.org/10.1109/IGARSS.2012.6351205.

Tomppo, E., Ronoud, G., Antropov, O., Hytönen, H., Praks, J., 2021. Detection of forest windstorm damages with multitemporal SAR Data—A case study: Finland. Remote Sens. 13, 383. https://doi.org/10.3390/rs13030383.

Udali, A., Lingua, E., Persson, H.J., 2021. Assessing forest type and tree species classification using Sentinel-1 C-band SAR data in southern Sweden. Remote Sens. 13, 3237. https://doi.org/10.3390/rs13163237.

Ulander, L.M.H., Smith, G., Eriksson, L., Folkesson, K., Fransson, J.E.S., Gustavsson, A., Hallberg, B., Joyce, S., Magnusson, M., Olsson, H., Persson, A., Walter, F., 2005. Mapping of wind-thrown forests in Southern Sweden using space- and airborne SAR. In: Proceedings. 2005 IEEE International Geoscience and Remote Sensing Symposium, 2005. IGARSS '05. Presented at the 2005 IEEE International Geoscience and Remote Sensing Symposium, 2005. IGARSS '05., IEEE, Seoul, Korea, pp. 3619–3622. https://doi.org/10.1109/IGARSS.2005.1526631.

Vaglio Laurin, G., Puletti, N., Tattoni, C., Ferrara, C., Pirotti, F., 2021. Estimated biomass loss caused by the vaia windthrow in northern Italy: evaluation of active and passive remote sensing options. Remote Sens. 13, 4924. https://doi.org/10.3390/rs13234924.

Vorovencii, I., 2014. Detection of environmental changes due to windthrows using landsat 7 ETM+ satellite images. Environ. Eng. Manag. J. 13, 565–576. https://doi.org/10.30638/eemj.2014.060.

Wang, F., Xu, Y.J., 2010. Comparison of remote sensing change detection techniques for assessing hurricane damage to forests. Environ. Monit. Assess. 162, 311–326. https://doi.org/10.1007/s10661-009-0798-8.

Wu, L., Wang, H., Li, Y., Guo, Z., Li, N., 2021. A novel method for layover detection in mountainous areas with SAR images. Remote Sens. 13, 4882. https://doi.org/10.3390/rs13234882.

Zoltán, L., Friedl, Z., Packskó, V., Orbán, I., Tanács, E., Magyar, B., Kristóf, D., Standovár, T., 2021. Application of Sentinel-1 radar data for mapping ice disturbance in a forested area. Eur. J. Remote Sens. 54, 569–588. https://doi.org/10.1080/22797254.2021.1982407.